

מכון ויצמן למדע

WEIZMANN INSTITUTE OF SCIENCE



Reconstructing Neoproterozoic seawater chemistry from early diagenetic dolomite

Document Version:

Accepted author manuscript (peer-reviewed)

Citation for published version:

Crockford, PW, Kunzmann, M, Blättler, CL, Kalderon-Asael, B, Murphy, JG, Ahm, A-S, Sharoni, S, Halverson, GP, Planavsky, NJ, Halevy, I & Higgins, JA 2021, 'Reconstructing Neoproterozoic seawater chemistry from early diagenetic dolomite', *Geology (Boulder)*, vol. 49, no. 4, pp. 442-446.
<https://doi.org/10.1130/G48213.1>

Total number of authors:

11

Digital Object Identifier (DOI):

[10.1130/G48213.1](https://doi.org/10.1130/G48213.1)

Published In:

Geology (Boulder)

License:

Other

General rights

@ 2020 This manuscript version is made available under the above license via The Weizmann Institute of Science Open Access Collection is retained by the author(s) and / or other copyright owners and it is a condition of accessing these publications that users recognize and abide by the legal requirements associated with these rights.

How does open access to this work benefit you?

Let us know @ library@weizmann.ac.il

Take down policy

The Weizmann Institute of Science has made every reasonable effort to ensure that Weizmann Institute of Science content complies with copyright restrictions. If you believe that the public display of this file breaches copyright please contact library@weizmann.ac.il providing details, and we will remove access to the work immediately and investigate your claim.

1 Reconstructing Neoproterozoic seawater chemistry from early 2 diagenetic dolomite

3
4 **Peter Crockford^{1,2}, Marcus Kunzmann³, Clara Blättler⁴, Boriana Kalderon-Asael⁵, Jack
5 Murphy², Anne-Sofie Ahm², Shlomit Sharoni¹, Galen Halverson⁶, Noah Planavsky⁵, Itay
6 Halevy¹, John Higgins²**

7
8 *¹Weizmann Inst. of Science, 76100, Israel*

9 *²Dept. Geosciences, Princeton University, NJ, 08544, USA*

10 *³CSIRO, Kensington, WA 6151, Australia*

11 *⁴Dept. Geophysical Sciences, University of Chicago, IL, 60637, USA*

12 *⁵Dept. Geology and Geophysics, Yale University, CT, 06511, USA*

13 *⁶Dept. Earth and Planetary Sciences, McGill University, QC, H3A 0E8, Canada*

14 15 **Abstract**

16 The pairing of Ca and Mg isotopes ($\delta^{44/40}\text{Ca}$, $\delta^{26}\text{Mg}$) has recently emerged as a useful tracer to
17 understand the environmental information preserved in shallow marine carbonates. Here we
18 apply a Ca and Mg isotopic framework, with analyses of C and Li isotopes, to late Tonian
19 dolostones, to infer seawater chemistry across this critical interval of Earth history. We
20 investigated the ca. 735 Ma Coppercap Fm. in northwestern Canada, a unit that preserves large
21 shifts in carbonate $\delta^{13}\text{C}$ values that have been utilized in global correlations and have canonically
22 been explained through large shifts in organic carbon burial. Under the backdrop of these $\delta^{13}\text{C}$
23 shifts, we observe positive excursions in $\delta^{44/40}\text{Ca}$ and $\delta^7\text{Li}$ values that are mirrored by a negative
24 excursion in $\delta^{26}\text{Mg}$ values. We argue that this covariation is due to early diagenetic
25 dolomitization of aragonite through interaction with contemporaneous seawater under a
26 continuum of fluid- to sediment-buffered conditions. We then use this framework to show that
27 Tonian seawater was likely characterized by a low $\delta^7\text{Li}$ value of $\sim 13\text{‰}$ ($\sim 18\text{‰}$ lower than
28 modern seawater), a consequence of a different Li cycle than today. In contrast, $\delta^{13}\text{C}$ values
29 across our identified fluid-buffered interval are similar to modern seawater. These observations

30 suggest that factors other than shifts to global seawater chemistry are likely responsible for such
31 isotopic variation.

32 **Introduction**

33 Developing a record of seawater chemistry for the majority of Earth's past is dependent
34 on estimating seawater composition from shallow-water (often dolomitized) carbonates.
35 Extracting such global information requires consideration of local processes that decouple
36 shallow-water environments from the global ocean, as well as diagenetic alteration ([Banner and
37 Hanson, 1990](#); [Boudreau, 2003](#); [Swart, 2008](#), [Hoffman and Lamothe, 2019](#)). Despite progress
38 identifying characteristic isotopic markers of early marine diagenesis in carbonates ([Higgins et
39 al., 2018](#); [Ahm et al., 2018](#)), ancient strata that show coherent geochemical stratigraphic
40 variability are rarely interpreted within alternative diagenetic frameworks. One interval of Earth
41 history known for high amplitude $\delta^{13}\text{C}$ variations is the Tonian Period. Based on the apparent
42 preservation of these variations in multiple successions of the same age, the canonical
43 interpretation is that they record contemporaneous shifts to global marine dissolved inorganic
44 carbon (DIC) ([Och and Shields-Zhou, 2013](#)). However, this view has recently been challenged
45 by a comprehensive isotopic dataset spanning the Otavi carbonate platform and slope succession
46 in Namibia which shows significant spatial heterogeneity in $\delta^{13}\text{C}$ values across platform to basin
47 transects, suggesting inner platform records may often better reflect local processes versus global
48 seawater ([Hoffman and Lamothe, 2019](#)).

49 One approach to further understand the geochemical information in dolomites such as
50 those referenced above, is coupled Ca and Mg isotopes ([Higgins et al., 2018](#); [Ahm et al., 2018](#);
51 [Fantle and DePaolo, 2007](#); [Fantle and Higgins, 2014](#)). Early diagenetic Ca isotopic variability in
52 carbonates predominantly arises due to sensitivity to water-rock ratios, precipitation rate and

53 degree of recrystallization or neomorphism. While additional factors, such as temperature and
54 salinity also impact Ca isotope fractionation between minerals and solution, in general, aragonite
55 and calcite precipitated rapidly (e.g., relevant timescales to the water column) are depleted in
56 ^{44}Ca relative to seawater Ca by $\sim 1.5\text{‰}$ and $\sim 0.9\text{‰}$, respectively (cf. [Gussone et al., 2005](#)).
57 However, slow rates of recrystallization and neomorphism that are characteristic of early marine
58 diagenesis do not significantly fractionate Ca isotopes ([Fantle and DePaolo, 2007](#)). In contrast,
59 dolomite is $\sim 2\text{‰}$ more depleted in ^{26}Mg than dolomitizing solutions ([Higgins and Schrag, 2010](#);
60 [Fantle and Higgins, 2014](#)). As a result, depending on Mg availability in pore-fluids, Mg can be
61 isotopically distilled during dolomitization. Together these systems offer the ability to
62 discriminate between Mg-replete fluid-buffered conditions (high $\delta^{44/40}\text{Ca}$, low $\delta^{26}\text{Mg}$; where the
63 chemistry of the carbonate mineral is dictated by the chemistry of the diagenetic fluid) and Mg-
64 poor sediment-buffered conditions (low $\delta^{44/40}\text{Ca}$, high $\delta^{26}\text{Mg}$, where the chemistry of the
65 carbonate mineral is dictated by the chemistry of the sediment) of dolomite formation. Recently,
66 results from [Dellinger et al. \(2020\)](#) suggests that this diagenetic framework can be extended to
67 Li. Here, we apply this approach to reconstruct aspects of Tonian seawater chemistry with
68 implications for the interpretation of shallow marine carbonate records.

69 **Materials and Methods**

70 We analyzed samples from the Coppercap Formation (Fm.) of the Windermere
71 Supergroup (base of section at $64^{\circ}37'49.2''\text{N}$ $129^{\circ}42'56.8''\text{W}$) in northwestern Canada ([Fig. 1](#);
72 [Aitken, 1981](#); Data Repository). The study area exposed ~ 100 m of a ~ 125 m section, consisting
73 of dolomitic carbonates dominated by matrix-supported debris flow deposits with cm-scale
74 intraclasts (dolofloatstone) and doloturbidite facies with m-scale fining-upward cycles, deposited
75 in a km-scale fault-bound sub-basin ([Fig. 1](#)). In total, 62 $\delta^{44/40}\text{Ca}$ and 66 $\delta^{26}\text{Mg}$ measurements

76 along with trace element analyses were performed at Princeton University following methods of
77 Higgins et al. (2018), 58 $\delta^7\text{Li}$ measurements were performed in the Yale Geochemistry Center
78 following methods of Dellinger et al. (2020), and 67 $\delta^{13}\text{C}$ and $\delta^{18}\text{O}$ measurements were
79 performed at McGill University following methods of Wörndle et al. (2019) (Data Repository).

80 **Results**

81 Basal section $\delta^{13}\text{C}$ values begin at -5‰ V-PDB but rise to 0‰ by 45 m, likely correlating
82 with the Russøya anomaly (Halverson et al., 2018). Values stay at 0‰ until ~ 100 m where they
83 progress toward $+4\text{‰}$. At the same time, $\delta^{44/40}\text{Ca}$ values display $>1\text{‰}$ of variation with values as
84 low as -1.33‰ (relative to modern seawater) in the lower part of the section (e.g., at 40.5 m),
85 increase to -0.25‰ (at 72.6 m), and then return to values near -1‰ at the top of the section (Fig.
86 1). A similar pattern in $\delta^{44/40}\text{Ca}$ is observed for $\delta^7\text{Li}$ values but with a range of $\sim 12\text{‰}$, beginning
87 at $\sim +1\text{‰}$ (relative to L-SVEC) at the base of the section, increasing to almost $+13\text{‰}$ at 80 m and
88 then declining to $+6\text{‰}$ (Fig. 1). Spanning $\sim 1.4\text{‰}$, $\delta^{26}\text{Mg}$ values mirror $\delta^{44/40}\text{Ca}$ and $\delta^7\text{Li}$ trends,
89 beginning at -1.2‰ (relative to Dead Sea Mg; DSM-3), decreasing to -1.8‰ in the middle of
90 the section and then increasing toward the top of the section (Fig. 1).

91 **Discussion**

92 Stratigraphic covariation between $\delta^{44/40}\text{Ca}$, $\delta^{26}\text{Mg}$ and $\delta^7\text{Li}$ values in the Coppercap
93 Fm. (Data Repository) could either result from synchronous shifts to global Li, Ca, and Mg
94 cycles, or from variability in the style and extent of diagenesis. While it is possible the
95 residence times of Ca, Mg and Li were similar across this interval, leading to covarying shifts
96 in these systems, this is unlikely given their large differences today (Ca ~ 0.5 -1 Ma, Fantle and
97 Tipper, 2014; Mg ~ 10 Ma, Higgins and Schrag, 2015; Li ~ 1.2 Ma, Misra and Froelich, 2012).
98 Moreover, mechanisms to explain the amplitude of observed signals and covariation between

99 any two systems, fail to explain all three. For $\delta^7\text{Li}$, possible global mechanisms include: 1)
100 changes to congruency of continental silicate weathering (Dellinger et al., 2014), 2) varying
101 clay particle-fluid interactions in Li sinks (Li and West, 2014), 3) changes in the flux ratio
102 between high and low temperature hydrothermal fluids (Chan et al., 2002), and 4) changes in
103 carbonate polymorph of primary precipitates (Marriott et al., 2004). However, all of these
104 mechanisms to explain $\delta^7\text{Li}$ trends fail to explain covariation with, and the magnitude of,
105 coeval $\delta^{44/40}\text{Ca}$ and $\delta^{26}\text{Mg}$ values. This is clearly demonstrated through $\delta^{26}\text{Mg}$ values, where
106 assuming that dolomite formation was secondary, the majority of Mg must have been
107 incorporated after primary precipitates formed and should display variation independent of
108 $\delta^7\text{Li}$ and $\delta^{44/40}\text{Ca}$ trends.

109 The above arguments motivate alternative explanations for stratigraphic trends in the
110 Coppercap Fm. Field observations favor an early-marine over late-stage diagenesis
111 interpretation. For example, no heterogeneity in sedimentary facies that may have facilitated late-
112 stage diagenetic fluid flow are apparent in the study area. Moreover, geochemical variability in
113 the Coppercap Fm. occurs over tens of meters and not broader spatial scales characteristic of
114 late-stage diagenesis (James and Jones, 2015). In addition, the scale of geochemical stratigraphic
115 variability and the observation of heavy $\delta^{44/40}\text{Ca}$ values are unlikely features produced through
116 late-stage diagenesis. Therefore, we interpret observed geochemical signals in the context of
117 early marine diagenesis and apply a numerical model following Ahm et al. (2018), to constrain
118 the boundary conditions of the alteration.

119 Our application of the model is influenced by observations from a modern carbonate
120 platform (Henderson et al., 1999; Higgins et al., 2018; Dellinger et al., 2020) and simulates the
121 dissolution of primary Ca carbonate and re-precipitation as dolomite along a flow path with an

122 evolving fluid composition. Due to the susceptibility of carbonate $\delta^{18}\text{O}$ values to reset through
123 any fluid interaction, they are less likely to constrain early marine diagenesis and are omitted
124 from further consideration. Model outputs are presented as fields in isotopic cross-plot space
125 between end-member compositions defined by the geochemistry of the primary sediment and the
126 diagenetic dolomite, and between sediment-buffered and fluid-buffered trajectories—of the
127 isotopic systems plotted—that connect end-member compositions (Fig. 2). Model solutions are
128 achieved through estimating the Ca, Li and Mg concentrations and isotopic compositions of the
129 primary sediment and then finding the diagenetic fluid composition required for the most
130 consistent fit to the measured dolomite data across all phase-spaces (Fig. 2; Data Repository).
131 Departures of data points from the predicted model solution may indicate spatio-temporal
132 heterogeneity in the geochemistry of the primary sediment or of the dolomitizing fluid, which is
133 not resolved by the model. Importantly, because the model does not explicitly account for several
134 C-fractionating processes (e.g., aerobic/anaerobic respiration of organic matter or
135 methanogenesis), it is not expected to capture the entire distribution of observed $\delta^{13}\text{C}$ variability
136 in sediment-buffered carbonates.

137 Based on our model fit to the data (Fig. 2), we argue that results best reflect diagenetic
138 processes rather than global seawater variation (Data Repository). From minimum $\delta^{44/40}\text{Ca}$
139 values and the range of observed $\delta^7\text{Li}$ values, we surmise that the initial carbonate mineral was
140 aragonite, which was then altered by a dolomitizing fluid (Blättler and Higgins, 2017; Marriott et
141 al., 2004). However, we argue that the geochemistry of the dolomitizing fluid was different for
142 the lower portion of the section versus middle and upper portions. Above ~50 m, dolomitization
143 by Tonian seawater (i.e., the same fluid from which the original aragonite formed) places the
144 measured data on model arrays that are well explained by a continuum of fluid- to sediment-

145 buffered conditions that display similar diagnostic isotopic systematics to modern carbonates that
146 have undergone early marine diagenesis (Higgins et al., 2018; Dellinger et al., 2020). Seawater
147 as the dolomitizing fluid is consistent with the Coppercap Fm.'s foreslope-like environment,
148 which has a high potential for open-system fluid-buffered diagenesis by seawater (Hoffman and
149 Lamothe, 2019). The fluid-buffered samples (~50-90 m) suggest that Tonian seawater had a $\delta^7\text{Li}$
150 value of ~13‰, a near-modern $\delta^{44/40}\text{Ca}$ value (0‰), and enough Mg that dolomitization did not
151 appreciably distill Mg isotopes (Fig. 2). The isotopic composition of the sediment-buffered
152 interval (~90-125 m) is consistent with aragonite that precipitated from the proposed Tonian
153 seawater, followed by dolomitization during early marine diagenesis under relatively closed-
154 system conditions that allowed for Mg drawdown and Mg-isotopic distillation in the diagenetic
155 fluid.

156 Data from the lower half of the section (~0-50 m) fall off the arrays that explain the
157 variation in the upper half of the section, displaying lower $\delta^{44/40}\text{Ca}$ and $\delta^7\text{Li}$ values (Fig. 2). The
158 isotopic composition of these samples is well-explained by sediment-buffered diagenesis of
159 aragonite that formed out of Tonian seawater, by a dolomitizing fluid that was a mixture of
160 brackish groundwater and Tonian seawater (Fig. S7). We suggest that groundwater flow through
161 the carbonate sediments on the shelf and slope resulted in a relatively Mg- and Li-poor, CaCO_3 -
162 saturated solution, the mixing of which with the proposed Tonian seawater, produces a
163 dolomitizing fluid that well explains the lower half of the section (Data Repository). It seems less
164 plausible that the dolomitizing fluid of the lower half of the section was purely seawater of a
165 different chemical and isotopic composition, given the required changes in the concentrations
166 and/or isotopic compositions, and the time available to affect these changes (Data Repository).

167 Although we contend that chemostratigraphic variability in the Coppercap Fm. reflects
168 variable diagenetic conditions and not variations in seawater chemistry, this analysis still yields
169 important insights into late Tonian Li and C cycles. Across the fluid-buffered interval, $\delta^7\text{Li}$
170 values approach $\sim 13\text{‰}$, which we argue is likely a close approximation of the $\delta^7\text{Li}$ composition
171 of late Tonian seawater (Dellinger et al., 2020). A $\delta^7\text{Li}$ of $\sim 13\text{‰}$ is significantly different from
172 modern seawater (31‰ ; Tomascak, 2004), possibly a consequence of lower riverine $\delta^7\text{Li}$ values
173 due to more congruent continental silicate weathering before the rise of land plants (Kalderson et
174 al., 2016) and potentially analogous to extreme weathering intervals of the Phanerozoic such as
175 the Permian-Triassic extinction (Sun et al., 2018). Additionally, the Precambrian ocean would
176 have been silica-rich (Drever, 1974) due to the absence of silicifying marine organisms, favoring
177 authigenic clay formation (Isson et al., 2020). Since authigenic clay formation in marine
178 sediments and during off-axis alteration are the major Li sinks (Misra and Froelich, 2012),
179 increased clay formation would likely result in a lower seawater Li concentration. Lower
180 seawater Li concentrations would favor near-quantitative Li uptake in marine sediments and off-
181 axis hydrothermal systems, muting the effect of preferential ^6Li uptake in these environments
182 (Chan et al., 2002), with the net effect of lowering Tonian $\delta^7\text{Li}$ values compared to Cenozoic
183 seawater (Misra and Froelich, 2012).

184 The fluid-buffered interval of the Coppercap Fm. can constrain the Tonian marine DIC
185 reservoir, too. Carbonate $\delta^{13}\text{C}$ values across these intervals are indistinguishable from modern
186 DIC at $\sim 0\text{‰}$ (Fig. 1). In contrast, large variability (-5‰ to $+4\text{‰}$) is observed across sediment-
187 buffered intervals. Given the isotopic evidence for diagenetic alteration of major constituents of
188 the carbonate rock (Ca, Mg), it seems reasonable that C would have been subjected to a similar
189 diagenetic fate. Variation of $\delta^{13}\text{C}$ values in the sediment-buffered intervals may have resulted

190 from organic matter remineralization or methanogenesis in the sediments or from variable
191 degrees of local C-isotope distillation of DIC across the platform (Swart, 2008; Geyman and
192 Maloof, 2019). In contrast, the fluid-buffered intervals may offer a more robust picture of Tonian
193 seawater carbonate chemistry.

194 Evaluation of local versus global controls on chemostratigraphic records in shallow
195 marine carbonates may be achieved by wider application of the paired Ca-Mg isotope
196 framework. This evaluation may be best executed by targeting environments with the greatest
197 potential to record seawater-buffered early marine diagenesis (i.e., the flanks of carbonate
198 platforms and slopes; Hoffman and Lamothe, 2019). If identified fluid-buffered intervals display
199 geochemical variability (e.g., $\delta^{13}\text{C}$, $\delta^7\text{Li}$, $\delta^{44/40}\text{Ca}$, $\delta^{26}\text{Mg}$) similar to sediment-buffered intervals,
200 then this will provide confidence in shallow marine carbonate archives as records of seawater
201 geochemical evolution. However, if a significant offset between fluid- and sediment-buffered
202 intervals is the norm, a more thorough screening of the existing shallow marine carbonate record
203 to identify fluid-buffered intervals will be necessary to reconstruct the secular evolution of
204 seawater chemistry. In the case of the Coppercap Fm., results suggest that Tonian marine DIC
205 $\delta^{13}\text{C}$ may not have varied to the degree that is suggested by shallow marine carbonate archives,
206 adding to a growing call for a reinterpretation of such records.

207

208 **Acknowledgements:** PWC acknowledges support from NSERC CREATE CATP program, the
209 Agouron Inst. and McGill University. GPH acknowledges support from NSERC. IH
210 acknowledges support from ERC Grant #755053. JAH, CLB Simons Foundation Award
211 #339006, NJP acknowledges support from the Alternative Earths NASA Astrobiology Inst.

212

213

214 **References:**

- 215 1. Banner, J.L. and Hanson, G.N., 1990, Calculation of simultaneous isotopic and trace element variations
216 during water-rock interaction with applications to carbonate diagenesis: *Geochimica et Cosmochimica*
217 *Acta*, 54(11), pp.3123-3137.
- 218 2. Boudreau, B.P., 1997, Diagenetic models and their implementation: Springer vol. 505.
- 219 3. Swart, P.K., 2008, Global synchronous changes in the carbon isotopic composition of carbonate sediments
220 unrelated to changes in the global carbon cycle: Proceedings of the National Academy of
221 Sciences, 105(37), pp.13741-13745.
- 222 4. Hoffman, P.F. and Lamothe, K.G., 2019, Seawater-buffered diagenesis, destruction of carbon isotope
223 excursions, and the composition of DIC in Neoproterozoic oceans: Proceedings of the National Academy of
224 Sciences, 116(38), pp.18874-18879.
- 225 5. Higgins, J.A., et al., 2018, Mineralogy, early marine diagenesis, and the chemistry of shallow-water
226 carbonate sediments: *Geochimica et Cosmochimica Acta*, 220, pp.512-534.
- 227 6. Ahm, A.S.C., Bjerrum, C.J., Blättler, C.L., Swart, P.K. and Higgins, J.A., 2018, Quantifying early marine
228 diagenesis in shallow-water carbonate sediments: *Geochimica et Cosmochimica Acta*, 236, pp.140-159.
- 229 7. Och, L.M. and Shields-Zhou, G.A., 2012, The Neoproterozoic oxygenation event: environmental
230 perturbations and biogeochemical cycling: *Earth-Science Reviews*, 110(1-4), pp.26-57.
- 231 8. Fantle, M.S. and DePaolo, D.J., 2007, Ca isotopes in carbonate sediment and pore fluid from ODP Site
232 807A: the Ca²⁺ (aq)-calcite equilibrium fractionation factor and calcite recrystallization rates in
233 Pleistocene sediments: *Geochimica et Cosmochimica Acta*, 71(10), pp.2524-2546.
- 234 9. Fantle, M.S. and Higgins, J., 2014, The effects of diagenesis and dolomitization on Ca and Mg isotopes in
235 marine platform carbonates: implications for the geochemical cycles of Ca and Mg: *Geochimica et*
236 *Cosmochimica Acta*, 142, pp.458-481.
- 237 10. Gussone, N., Böhm, F., Eisenhauer, A., Dietzel, M., Heuser, A., Teichert, B.M., Reitner, J., Wörheide, G.
238 and Dullo, W.C., 2005, Calcium isotope fractionation in calcite and aragonite: *Geochimica et*
239 *Cosmochimica Acta*, 69(18), pp.4485-4494.
- 240 11. Higgins, J.A. and Schrag, D.P., 2010, Constraining magnesium cycling in marine sediments using
241 magnesium isotopes: *Geochimica et Cosmochimica Acta*, 74(17), pp.5039-5053.
- 242 12. Dellinger, M., Hardisty, D.S., Planavsky, N.H., Gill, B.C., Kalderon-Asael, B., Asael, D., Croissant, T.,
243 Swart, P.K. and West, A.J., 2020, The effects of diagenesis on lithium isotope ratios of shallow marine
244 carbonates: *American Journal of Science*, 320(2) p.150-184.
- 245 13. Aitken, J.D., 1981, Stratigraphy and sedimentology of the Upper Proterozoic Little Dal Group, Mackenzie
246 Mountains, Northwest Territories: Proterozoic basins of Canada: Geological Survey of Canada
247 Paper, 81(10), pp.47-71.
- 248 14. Wörndle, S., Crockford, P.W., Kunzmann, M., Bui, T.H. and Halverson, G.P., 2019, Linking the Bitter
249 Springs carbon isotope anomaly and early Neoproterozoic oxygenation through I/[Ca+ Mg]
250 ratios: *Chemical Geology*, 524, pp.119-135.
- 251 15. Halverson, G.P., Porter, S.M. and Gibson, T.M., 2018, Dating the late Proterozoic stratigraphic
252 record: *Emerging Topics in Life Sciences*, 2(2), pp.137-147.
- 253 16. Fantle, M.S. and Tipper, E.T., 2014, Calcium isotopes in the global biogeochemical Ca cycle: Implications
254 for development of a Ca isotope proxy: *Earth-Science Reviews*, 129, pp.148-177.
- 255 17. Higgins, J.A. and Schrag, D.P., 2015, The Mg isotopic composition of Cenozoic seawater—evidence for a
256 link between Mg-clays, seawater Mg/Ca, and climate: *Earth and Planetary Science Letters*, 416, pp.73-81.
- 257 18. Misra, S. and Froelich, P.N., 2012, Lithium isotope history of Cenozoic seawater: changes in silicate
258 weathering and reverse weathering: *Science*, 335(6070), pp.818-823.
- 259 19. Dellinger, M., Gaillardet, J., Bouchez, J., Calmels, D., Galy, V., Hilton, R.G., Louvat, P. and France-
260 Lanord, C., 2014, Lithium isotopes in large rivers reveal the cannibalistic nature of modern continental
261 weathering and erosion: *Earth and Planetary Science Letters*, 401, pp.359-372.
- 262 20. Li, G. and West, A.J., 2014, Evolution of Cenozoic seawater lithium isotopes: Coupling of global
263 denudation regime and shifting seawater sinks: *Earth and Planetary Science Letters*, 401, pp.284-293.
- 264 21. Chan, L.H., Alt, J.C. and Teagle, D.A., 2002, Lithium and lithium isotope profiles through the upper
265 oceanic crust: a study of seawater-basalt exchange at ODP Sites 504B and 896A: *Earth and Planetary*
266 *Science Letters*, 201(1), pp.187-201.

- 267 22. Marriott, C.S., Henderson, G.M., Crompton, R., Staubwasser, M. and Shaw, S., 2004, Effect of mineralogy,
268 salinity, and temperature on Li/Ca and Li isotope composition of calcium carbonate: *Chemical*
269 *Geology*, 212(1-2), pp.5-15.
- 270 23. James, N.P. and Jones, B., 2015, *Origin of carbonate sedimentary rocks*. John Wiley & Sons.
- 271 24. Henderson, G.M., Slowey, N.C. and Haddad, G.A., 1999, Fluid flow through carbonate platforms:
272 constraints from $^{234}\text{U}/^{238}\text{U}$ and Cl^- in Bahamas pore-waters: *Earth and Planetary Science Letters*, 169(1-
273 2), pp.99-111.
- 274 25. Blättler, C.L. and Higgins, J.A., 2017, Testing Urey's carbonate–silicate cycle using the calcium isotopic
275 composition of sedimentary carbonates: *Earth and Planetary Science Letters*, 479, pp.241-251.
- 276 26. Tomascak, P.B., 2004, Developments in the understanding and application of lid isotopes in the earth and
277 planetary sciences: *Reviews in Mineralogy and Geochemistry*, 55(1), pp.153-195.
- 278 27. Kalderon B., Planavsky, N., Asael, D. A Carbonate Li Isotope Record Throughout Earth History.
279 *Goldschmidt Yokohama (2016)*, Abstract.
- 280 28. Sun, H., Xiao, Y., Gao, Y., Zhang, G., Casey, J.F. and Shen, Y., 2018, Rapid enhancement of chemical
281 weathering recorded by extremely light seawater lithium isotopes at the Permian–Triassic
282 boundary: *Proceedings of the National Academy of Sciences*, 115(15), pp.3782-3787.
- 283 29. Drever, J.I., 1974, Geochemical model for the origin of Precambrian banded iron fms: *Geological Society*
284 *of America Bulletin*, 85(7), pp.1099-1106.
- 285 30. Isson, T.T., Planavsky, N.J., Coogan, L.A., Stewart, E.M., Ague, J.J., Bolton, E.W., Zhang, S., McKenzie,
286 N.R. and Kump, L.R., 2020, Evolution of the global carbon cycle and climate regulation on Earth: *Global*
287 *Biogeochemical Cycles*, 34(2).
- 288 31. Geyman, E.C. and Maloof, A.C., 2019, A diurnal carbon engine explains ^{13}C -enriched carbonates without
289 increasing the global production of oxygen: *Proceedings of the National Academy of Sciences*, 116(49),
290 pp.24433-24439.
- 291 32. Crockford, P.W., et al., 2016. Triple oxygen and multiple sulfur isotope constraints on the evolution of the
292 post-Marinoan sulfur cycle: *Earth and Planetary Science Letters*, 435, pp.74-83.
- 293 33. Rooney, A.D., Macdonald, F.A., Strauss, J.V., Dudás, F.Ö., Hallmann, C. and Selby, D., 2014, Re-Os
294 geochronology and coupled Os-Sr isotope constraints on the Sturtian snowball Earth: *Proceedings of the*
295 *National Academy of Sciences*, 111(1), pp.51-56.
- 296 34. Macdonald, F.A., Schmitz, M.D., Crowley, J.L., Roots, C.F., Jones, D.S., Maloof, A.C., Strauss, J.V.,
297 Cohen, P.A., Johnston, D.T. and Schrag, D.P., 2010, Calibrating the Cryogenian: *Science*, 327(5970),
298 pp.1241-1243.
- 299 35. MacLennan, S., Park, Y., Swanson-Hysell, N., Maloof, A., Schoene, B., Gebreslassie, M., Antilla, E.,
300 Tesema, T., Alene, M. and Haileab, B., 2018, The arc of the Snowball: U-Pb dates constrain the Islay
301 anomaly and the initiation of the Sturtian glaciation: *Geology*, 46(6), pp.539-542.
- 302

303 **Figure Captions:**

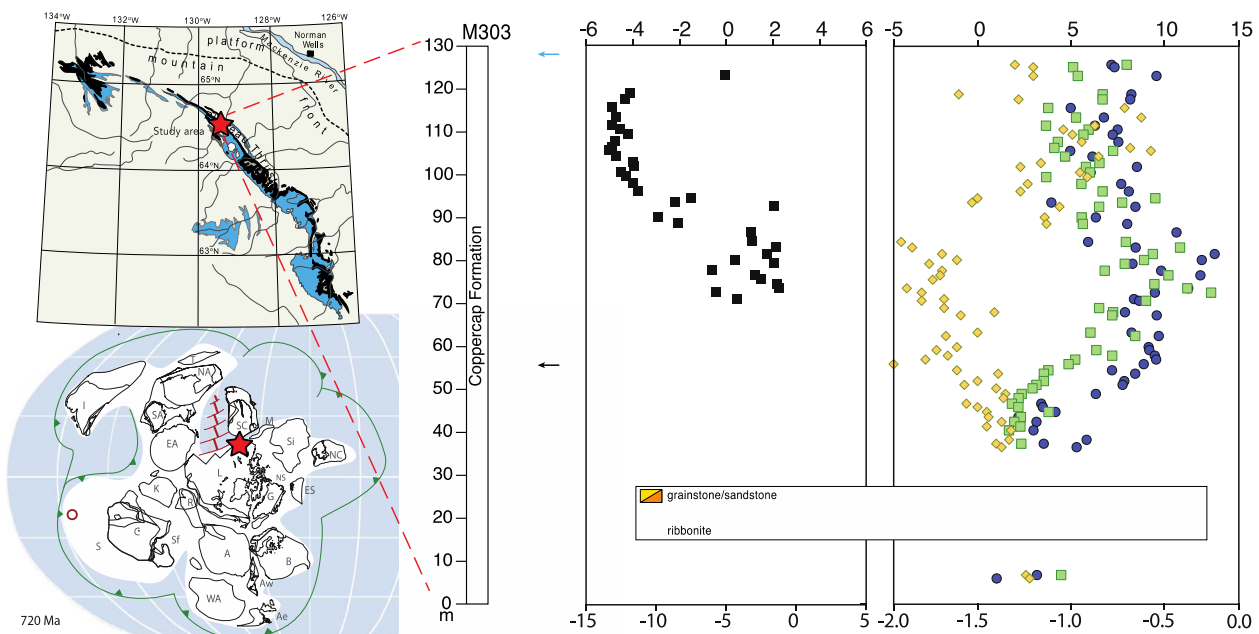
304 Figure 1. Map adapted from Crockford et al. (2016) and sedimentary facies stratigraphically
305 plotted with geochemical data. Errors on measurements are in the lower right corner of panels. In
306 black is a Re-Os date measured on a different Coppercap Fm. section (Rooney et al., 2014). In
307 blue are U-Pb dates correlated from the Ogilvie Mts. (upper date; Macdonald et al., 2010) and
308 Ethiopia (MacLennan et al., 2018).

309

310 Figure 2. $\delta^{26}\text{Mg}$, $\delta^7\text{Li}$ and $\delta^{44/40}\text{Ca}$ cross-plots with model solutions. Grid lines represent %
 311 alteration in 10% increments. Red stars represent the primary aragonite and blue lines represent
 312 the final diagenetic product. Blue diamonds are proposed Tonian seawater.

313

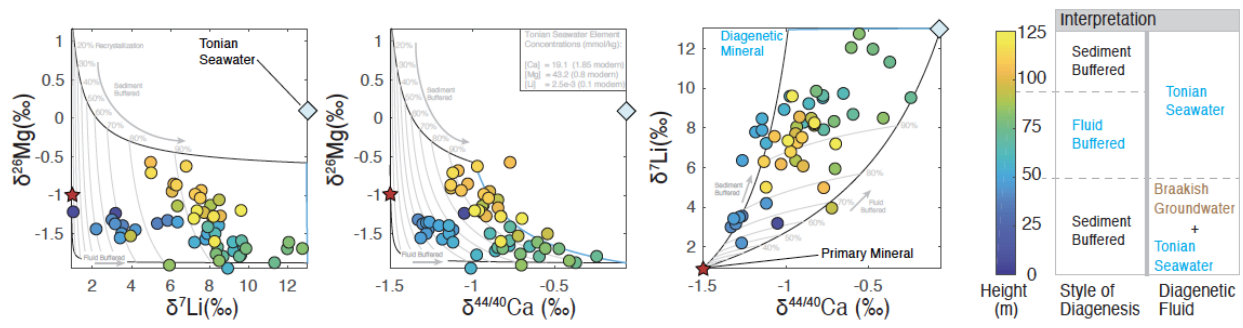
314 Fig. 1



315

316

317 Fig. 2



318

319

320

321 **GSA Data Repository:**

322 **Reconstructing Neoproterozoic seawater chemistry from early**
323 **diagenetic dolomite**

324

325 **Peter Crockford^{1,2}, Marcus Kunzmann³, Clara Blättler⁴, Boriana Kalderon-Asael⁵, Anne-**
326 **Sofie Ahm², Jack Murphy², Shlomit Sharoni¹, Galen Halverson⁶, Noah Planavsky⁵, Itay**
327 **Halevy¹, John Higgins²**

328

329 ¹*Weizmann Inst. of Science, 76100, Israel*

330 ²*Dept. Geoscience, Princeton University, NJ, 08544, USA*

331 ³*CSIRO, Kensington, WA 6151, Australia*

332 ⁴*Dept. Geophysical Sciences, University of Chicago, IL, 60637, USA*

333 ⁵*Dept. Geology and Geophysics, Yale University, CT, 06511, USA*

334 ⁶*Dept. Earth and Planetary Sciences, McGill University, QC, H3A 0E8, Canada*

335

336 **Supplementary Information**

337

338 *Isotopic notation*

339

340 All isotopic measurements are presented in delta notation following equation S1:

341

$$(S1) \delta^i M = ((R_{sample}/R_{standard}) - 1) \times 1000$$

343

344 Where superscript *i* represents 44/40, 26, 13, 18, 7 and *M* represents elements C, O, Mg, Ca, Li
345 and R represents isotopic ratios ⁴⁴Ca/⁴⁰Ca, ²⁶Mg/²⁴Mg, ¹³C/¹²C, ¹⁸O/¹⁶O, and ⁷Li/⁶Li.

346

347 *Carbon and oxygen isotopes*

348

349 In total, 66 samples were measured for carbon ($\delta^{13}\text{C}$) and oxygen ($\delta^{18}\text{O}$) isotopes from
350 the Coppercap Fm. Samples were first cut and then fresh surfaces were drilled with efforts made
351 to avoid small veins. With a Nu-Carb device, between 100-140 μg of drilled powders were then
352 dissolved in glass vials through the addition of H_3PO_4 at 70°C . Liberated $\text{CO}_{2(g)}$ was then
353 cryogenically isolated and analysed in dual-inlet mode on a Nu Perspective isotope ratio mass
354 spectrometer at McGill University. Isotopic ratios were measured against an in-house reference
355 gas and results are reported on the Vienna-Pee Dee Belemnite (V-PDB) scale. Uncertainty on
356 measurements (1σ) based on the long-term analyses of NCM and UQ-6 standards is $< 0.05\%$.

357

358 *Calcium and magnesium isotopes*

359

360 *Sample preparation*

361

362 In total, 61 samples were measured for calcium isotopes ($\delta^{44/40}\text{Ca}$) and 66 samples were
363 measured for magnesium isotopes ($\delta^{26}\text{Mg}$) in the Coppercap Fm. Carbonate powders from the
364 same aliquots utilized for carbon and oxygen isotopes were first weighed into 5 mg portions and

365 placed into cleaned 15 mL Corning centristar tubes. Samples were then dissolved into 0.1 N
366 buffered acetic acid ammonium hydroxide solution over four hours in a sonicator. Samples were
367 then centrifuged and aliquots of the supernatant were transferred into cleaned 15 mL Corning
368 centristar tubes. Aliquots of the bulk supernatants were then diluted ~30 times and calcium and
369 magnesium were separated in different runs via a Thermo-Dionex ICS-5000+ ion chromatograph
370 equipped with a fraction collector. Resultant calcium separates were then dried down and
371 redissolved into concentrated distilled nitric acid. Samples were then dried down and taken back
372 up into a volume of 2% nitric acid with the aim of having final solutions with a calcium
373 concentration of 2 ppm.

374 375 *Mass spectrometry*

376
377 Calcium and magnesium isotopic ratios were measured at Princeton University using a
378 Thermo Neptune plus multi collector inductively coupled plasma mass spectrometer (MC-
379 ICPMS). Samples were introduced via an ESI Apex-IR sample introduction system. For calcium
380 isotopes, $^{44}\text{Ca}/^{42}\text{Ca}$ isotopic ratios were measured through sample-standard bracketing and were
381 performed in medium resolution mode to avoid isobaric $^{87}\text{Sr}^{2+}$ and ArHH^+ interferences. Under
382 an assumption of no radiogenic ^{40}Ca excess (Caro et al., 2010), $^{44}\text{Ca}/^{40}\text{Ca}$ isotopic ratios were
383 calculated utilizing established kinetic fractionation laws (2.05; Young et al., 2002) and are
384 presented relative to modern seawater. Based on the long-term measurement of SRM-915b (n =
385 199) we report an external reproducibility (2σ) on measurements of 0.14‰ and obtained a value
386 for SRM-915b of 1.15‰ that is within error of previously published results (Heuser and
387 Eisenhauer, 2008). Magnesium isotope ratios ($^{26}\text{Mg}/^{24}\text{Mg}$) were measured in low resolution
388 mode and were also performed using sample standard bracketing. Results are presented relative
389 to Dead Sea Magnesium (DSM-3). Long term external precision (2σ) on magnesium isotope
390 results was determined through repeated measurements of the Cambridge-1 standard (-2.59 +/-
391 0.07‰ n = 19) and modern seawater (-0.82 +/- 0.14 ‰ n = 21). Both magnesium and calcium
392 isotopic results are presented as delta values and all results were plotted in three isotope space
393 ($^{26}\text{Mg}/^{24}\text{Mg}$ vs. $^{25}\text{Mg}/^{24}\text{Mg}$ and $^{44}\text{Ca}/^{42}\text{Ca}$ vs. $^{43}\text{Ca}/^{42}\text{Ca}$) to confirm that isotopic values fell
394 within typical mass-dependent variability.

395 396 *Lithium isotopes*

397 398 *Sample preparation*

399
400 The sample preparation and column chemistry for lithium isotope analysis were
401 performed in a PicoTrace class-10 clean laboratory at Yale University. Blank lithium levels for
402 each batch of samples were monitored and found to be negligible, at 0.00 % of the lithium in
403 samples and standards. Approximately 375 mg of carbonate powder from samples was utilized
404 for Li isotope measurements. Powders were first leached in 1M ammonium acetate and washed
405 twice in 2X MQ2 H₂O to remove the lithium adsorbed or bound to secondary minerals. Powders
406 were then dissolved in three steps (4h, 2h and 10 minutes) into a 0.05N hydrochloric acid
407 solution, each time the sample being centrifuged for 5 minutes at 4000 rpm. Each supernatant
408 was then extracted into Teflon beakers, dried on a hot plate and redissolved in 6N HCl. Acid
409 splits were dried down and then dissolved in 1ml of 0.2N HCl before being loaded directly onto
410 2.7 ml Bio-Rad AG50W-X12 (200-400 mesh) cation exchange resin pre-cleaned with 6N HCl

411 and 2X MQ2 H₂O and preconditioned with 0.2N HCl. Lithium was released from the cation
 412 exchange resin through the addition of 0.2N HCl. After drying samples down, 5% HNO₃ was
 413 added to the samples by first adding distilled HNO₃ (left sealed on a hotplate at 60 °C for 30
 414 minutes) and then diluting it down with 2X MQ2 H₂O to the desired strength. A split of 100µl
 415 was taken out and then 900µl of 2X MQ2 H₂O was added to the splits and these solutions were
 416 used for lithium and sodium concentration checks in post column solutions.

417

418 *Mass spectrometry*

419

420 The lithium and sodium post column concentrations and the lithium isotopic composition
 421 were measured with a Thermo Finnigan Neptune Plus ICP-MS at Yale University. Lithium
 422 isotope data was collected at low resolution in 1 block, 50 cycles per block and 5 second
 423 integrations per cycle. For these measurements we used the standard-sample-standard bracketing
 424 technique using the L-SVEC standard and then calculated sample values based on the bracketing
 425 standard values. In order to monitor the long-term reproducibility of our procedure, standards
 426 were processed with each set of samples. A typical standard error of a single measurement is
 427 0.16 ‰. Unprocessed standard was employed as a drift monitor throughout each run giving a
 428 long-term external precision of 0.2 ‰ (1 σ), n=147. Column duplicates of samples typically fall
 429 within 0.26 ‰ (n=19). Geostandards after column chromatography give the following values: L-
 430 SVEC = 0.08 ± 0.52 ‰ (2σ) (n=19), BHVO-2 = 4.46 ± 0.55 ‰ (2σ) (n= 18) and Atlantic
 431 Seawater = 31.25 ± 0.51 ‰ (2σ) (n=13). Given that most of the samples had very low lithium
 432 concentrations and the standards were prepared to match those concentrations, the observed error
 433 is higher than maximum achievable in high concentration samples.

434

435 *Data Correlation*

436

437 Throughout the main text we refer to δ²⁶Mg, δ^{44/40}Ca and δ⁷Li values covarying. We
 438 arrive at this description through performing a Spearman rank correlation test. This test is a non-
 439 parametric measure of the dependence of two variables. We specifically performed a Spearman
 440 test and not a Pearson test because we did not assume a Gaussian distribution of our data. In all
 441 cases, we found a statistically (95% CI) significant correlation between δ²⁶Mg, δ^{44/40}Ca and δ⁷Li
 442 values, which is why we use the term covariation in the main text.

443

Table S1: Spearman r correlation test

| | Ca vs. Mg | Ca vs. Li | Li vs. Mg |
|-----------------------------|--------------------|--------------------|------------------|
| r | -0.3971 | -0.5192 | 0.6449 |
| 95% CI | -0.5964 to -0.1518 | -0.6910 to -0.2919 | 0.4449 to 0.7837 |
| P (two-tailed, approximate) | 0.002 | <.001 | <.001 |
| significant? (alpha = 0.05) | Yes | Yes | Yes |
| number of XY pairs | 60 | 57 | 52 |

444

445 *Description of diagenetic model*

446

447 To constrain the origin of geochemical signatures in the Coppercap Fm., we model
448 carbonate diagenesis and dolomitization using a numerical model of Ahm et al., (2018). Since
449 the geochemistry of the original carbonate precipitates of the Coppercap Fm. is not known and
450 because the initial model did not include Li, we modified the code of Ahm et al., (2018) to: 1)
451 ensure the chemistry of initial precipitates is consistent with our proposed seawater composition
452 and 2) added Li and Li isotopes into this modelling framework partially based on recent results
453 from the Bahamas by Dellinger et al., (2020) (see Taylor et al., 2018 for an alternative view on
454 the Li isotope fractionation factor into dolomite). This model provides predictions for the
455 geochemistry of the diagenetic fluid. It arrives at such predictions by finding model solutions
456 that provide the best fit to isotopic data from natural samples which we describe in more detail
457 below.

458 The model simulates early marine carbonate diagenesis through the dissolution of
459 primary calcium carbonate and re-precipitation of dolomite along a flow path. Again, a slight
460 modification to the code of Ahm et al., (2018) was made to ensure that original precipitates form
461 from a hypothesized seawater composition, which forms the basis of the diagenetic fluid that the
462 original precipitates recrystallize and diagenetically alter within. Based on observations from
463 modern carbonate platforms, we assume that the Coppercap Fm. was dolomitized during early
464 marine diagenesis within 100,000 yrs and use a reaction rate of 0.01% kyr⁻¹ and a fluid-flow rate
465 of 0.1 m yr⁻¹ (Table S2; Higgins et al., 2018). However, since we evaluate our model output in
466 cross-plot space, our model results are not significantly affected by changes in either reaction
467 rates or flow rates. Importantly, the model results with respect to lithium are sensitive to the
468 choice of Li partition coefficient into dolomite which to date has not been experimentally
469 determined at low temperatures. To achieve our best model fit we tuned this parameter finding a
470 value of 0.0005, however, increasing it up to ≈0.0015 still provided good fits to the data. This
471 ‘best fit’ partition coefficient range is potentially quite different from results of Dellinger et al.,
472 (2020) whose data could suggest a value closer to 0.008 in the Bahamas. While there are many
473 possibilities for this potential difference including differences in seawater chemistry (or
474 chemistry of the diagenetic fluid), temperature or partitioning calculations (cf., Langer et al.,
475 2015; 2020), these results highlight the much-needed continued effort to constrain environmental
476 controls on the lithium partition coefficient into dolomite.

477 The model outputs isotopic trajectories that represent mixtures of primary carbonates
478 (with a calculated composition from the prescribed seawater composition; see Table S2) and
479 diagenetic dolomites spanning a range of fluid- to sediment-buffered compositions. As a result,
480 the model output is a ternary phase-space between pairs of geochemical proxies that is defined
481 by the geochemistry of the primary sediment and fluid-buffered and sediment-buffered
482 trajectories, which terminate at 100% diagenetically altered end-member solutions. By
483 identifying the fluid- and sediment-buffered end-members that are consistent with data from
484 100% recrystallized samples (100% dolomite), we can use the model to infer the composition
485 of the diagenetic fluid and, therefore, of the primary sediment. That is, we overlay data from
486 the Coppercap Fm. and explore model solutions that can provide the best fit to the data, which
487 then allow us to explore the geochemistry of the diagenetic fluid. To ensure consistent
488 predictions of different proxies, the position and shape of the model phase space is constrained
489 by visually optimizing the percentage of alteration (+/- 20%) across all phase spaces. For
490 example, samples that fall into the 100% dolomitized phase-space of $\delta^{44/40}\text{Ca}$ versus $\delta^{26}\text{Mg}$
491 values, should also near 100% dolomitization in the phase-space $\delta^{44/40}\text{Ca}$ versus $\delta^7\text{Li}$ values.

492 Samples that are less than 100% recrystallized in model phase spaces are interpreted to
 493 only be partially altered during early marine diagenesis (Higgins et al., 2018). These samples are
 494 subsequently stabilized during later burial diagenesis in conditions that are sediment-buffered
 495 (i.e., much lower water-rock ratios), thus preserving the geochemical signals associated with
 496 early marine diagenesis. That is, our model does not assume that samples do not undergo
 497 subsequent diagenetic recrystallization during burial, simply that this recrystallization must have
 498 been sediment-buffered and would therefore preserve the geochemical signature of early marine
 499 diagenesis and not further alter the chemistry of the carbonate away from this early diagenetic
 500 composition.

501 An important final note, overlaying data from natural samples on model solutions will not
 502 yield perfect agreement. In other words, given the specified chemical and isotopic compositions
 503 of the original mineral and a diagenetic fluid, the idealized model predictions will not always
 504 agree with fine details in the data. For example, minor differences are expected in the degree of
 505 alteration of specific samples between isotope cross-plots. More major departures from 90-100%
 506 dolomitization contours of samples that are known to be fully dolomitized suggest that
 507 alternative explanations should be explored. This is an additional strength of this approach as it
 508 allows for the identification of samples or sample-intervals that may have been subjected to
 509 either different conditions, or additional processes that the model is unable to capture in a single
 510 simulation.

511
 512 Table S2: All model parameters.
 513

| Parameter | Definition | Value used in model | References |
|--------------------|---|---------------------|---|
| α_{Ca-Dol} | Ca isotopic fractionation factor for dolomitization | 1.000 | Jacobsen and Holmden, 2008; Fantle and DePaolo, 2007 |
| α_{Mg-Dol} | Mg isotopic fractionation factor for dolomitization | 0.9980 | Fantle and Higgins, 2014 |
| α_C-Dol | C isotopic fractionation factor for dolomitization | 1.0025 | Horita, 2014 |
| α_{Li-Dol} | Li isotopic fractionation factor for dolomitization | 1.000 | Dellinger et al., 2020 |
| K_{Li-Dol} | Li/Ca partition coefficient into dolomite | 0.0005 | - |
| $\alpha_{Ca-Arag}$ | Ca isotopic fractionation factor for aragonite | 0.9985 | Gussone et al., 2020 |
| $\alpha_{Mg-Arag}$ | Mg isotopic fractionation factor for aragonite | 0.9993 | Wang et al., 2013 |
| α_C-Arag | C isotopic fractionation factor for aragonite | 1.0027 | Romanek et al., 1992 |
| $\alpha_{Li-Arag}$ | Li isotopic fractionation factor for aragonite | 0.988 | Marriott et al., 2004; Dellinger et al., 2018; Pogge von Strandman et al., 2019 |
| $K_{Li-Arag}$ | Li/Ca partition coefficient into aragonite | 0.003 | Dellinger et al., 2020 |

| | | | |
|---------------|--|--|--|
| $K_{Mg-Arag}$ | Mg/Ca partition coefficient for aragonite | 0.0019 | Ahm et al. 2018 |
| R | Reaction rate | $1 \times 10^{-5} \text{ yr}^{-1}$ | Higgins et al., 2018; Swart et al., 1987 |
| u | Fluid advection rate | 0.01 m yr^{-1} | Henderson et al., 1999 |
| M_f | Chemical composition of diagenetic fluid (mmol/kg) | Ca = 19.1, Mg = 43.2, Li = 0.002 | Best-fit estimate in this study |
| M_s | Chemical composition of primary solid (aragonite) | Ca = 39.5%, C = 12%, Mg = 1.03%, Li = 0.03 ppm | Best-fit estimate in this study |
| δ_f | Isotopic composition of diagenetic fluid | $\delta^{44/40}\text{Ca} = 0.0\text{‰}$, $\delta^{26}\text{Mg} = 0.1\text{‰}$, $\delta^7\text{Li} = 13\text{‰}$ | Best-fit estimate in this study |
| δ_s | Isotopic composition of primary solid (aragonite) | $\delta^{44/40}\text{Ca} = -1.5\text{‰}$, $\delta^{26}\text{Mg} = -0.6\text{‰}$, $\delta^7\text{Li} = 1\text{‰}$ | Best-fit estimate in this study |

514

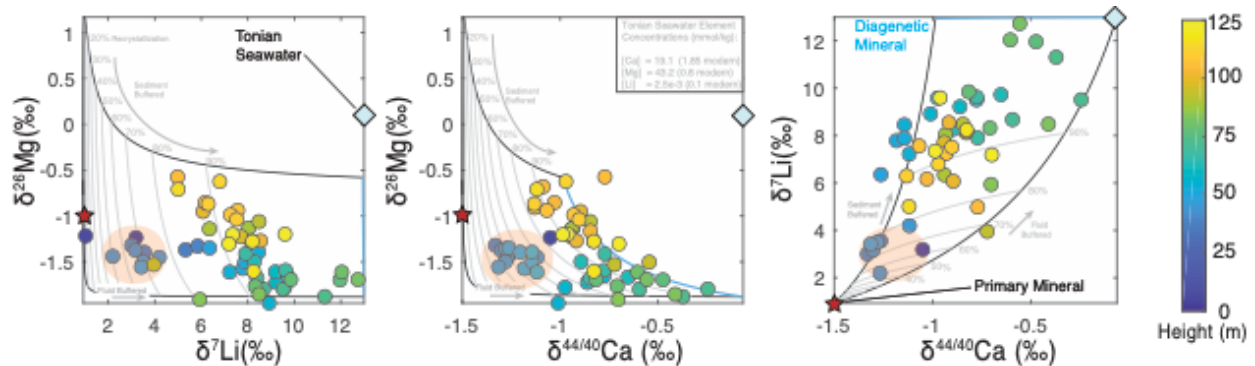
515 *Model fit to data from the Coppercap Fm.*

516

517 Our ability to fit diagenetic model solutions with geochemical data (see main text)
518 provides a compelling case for early marine diagenesis driving the majority of geochemical
519 variability observed in the Coppercap Fm. This is seen in Fig. 2 of the main text, which is also
520 replotted here as Fig. S1. In Fig. S1 it is shown that the upper and middle portions of the
521 Coppercap Fm. predominantly plot within the 80-100% diagenetically altered contours between
522 fluid and sediment buffered end-members, with the middle portion of the section clustering
523 toward the fluid buffered end-member and the top of the section clustering toward the sediment
524 buffered end-member in $\delta^{26}\text{Mg} - \delta^7\text{Li}$, $\delta^{26}\text{Mg} - \delta^{44/40}\text{Ca}$ and $\delta^7\text{Li} - \delta^{44/40}\text{Ca}$ cross-plot space.
525 However, many lower section samples do not fall within the >80% diagenetically altered
526 (dolomitized) field (Fig. S1). This observation of the lower samples can be explained by one of
527 three different possibilities: 1) samples in the lower portion of the section are not completely
528 dolomite and retain some of their original geochemistry and thus plot closer to the initial
529 aragonite, 2) lower samples underwent a slightly different diagenetic history than samples above
530 due to local shifts in fluid composition, or, 3) seawater chemistry changed and thus the
531 diagenetic fluid and initial aragonite geochemistry shifted between the lower samples and the
532 samples above. We can immediately rule out the first scenario, as all samples in the Coppercap
533 Fm. are dolomite (Table S9). Below, we explore the second and third scenarios outlined above in
534 detail.

535

536



537

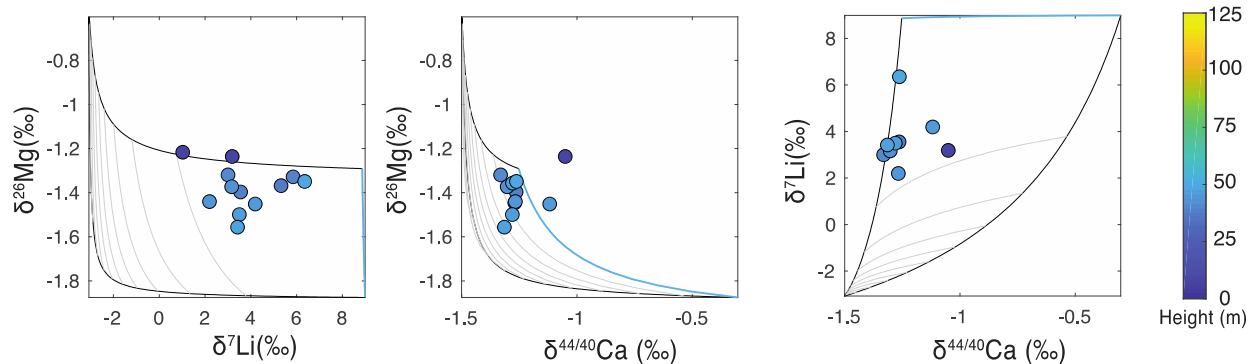
538

539

Figure S1: Figure 2 from the main text with $\delta^{26}\text{Mg} - \delta^7\text{Li}$, $\delta^{26}\text{Mg} - \delta^{44/40}\text{Ca}$ and $\delta^7\text{Li} - \delta^{44/40}\text{Ca}$ cross-plots of both model solutions and data from the Coppercap Fm. The colours of data points represent stratigraphic height. The primary

540 mineral (aragonite) is represented by the red star, the blue line corresponds to the diagenetic product (dolomite) and
 541 the light blue diamond represents the composition of Tonian seawater. Upper black curves on the left two panels and
 542 the left curves on the right-most panel represent sediment buffered trajectories. Lower black curves on the left two
 543 panels and the right curve on the right most panel represents fluid buffered trajectories. Grey contours represent %
 544 recrystallization from the primary mineral to the diagenetic product. In the case of the Coppercap Fm. this corresponds
 545 to aragonite at 0% and stoichiometric dolomite at 100%, with minor element compositions corresponding to aragonite
 546 that precipitated from our prescribed seawater composition and dolomite geochemistry from the Coppercap Fm. The
 547 peach-coloured field highlights data points from the lower portion of the Coppercap Fm., which are dolomite but do
 548 not plot close to the diagenetic (dolomite) end-member mineral composition. Such a model-measurement misfit
 549 requires exploration of alternative explanations.

550
 551 **Changes in seawater chemistry on the required timescale are unlikely.** We first consider the
 552 possibility that global seawater geochemistry shifted between the time of deposition of the lower
 553 samples to the time of deposition of the middle and upper samples in the Coppercap Fm. A
 554 change in seawater chemistry would have shifted the composition of the diagenetic fluid as well
 555 as shifted the original composition of the aragonite that we assume precipitated from it.
 556 Exploring diagenetic model phase spaces, we are able to generate solutions consistent with
 557 samples in the lower section (i.e., we can capture sample geochemistry within >80% dolomitized
 558 fields) by altering element concentrations in the diagenetic fluid (seawater) as well as its isotopic
 559 composition (Fig. S2). The most dramatic changes to fluid chemistry required are either through
 560 a reduction in [Ca] and/or a reduction in $\delta^{44/40}\text{Ca}$ values of the diagenetic fluid that dolomitized
 561 lower samples compared to the diagenetic fluid composition required for model solutions for
 562 samples in the middle and upper portions of the section (Table S3). We primarily focus on Ca in
 563 the discussion below, as much less significant shifts in diagenetic fluid [Mg], [Li] and $\delta^{26}\text{Mg}$
 564 values are required to achieve model fits.
 565



566
 567 Figure S2: $\delta^{26}\text{Mg}$ - $\delta^7\text{Li}$, $\delta^{26}\text{Mg}$ - $\delta^{44/40}\text{Ca}$ and $\delta^7\text{Li}$ - $\delta^{44/40}\text{Ca}$ cross-plots of both model solutions and data from the
 568 lower portion of the Coppercap Fm. The colours of data points represent stratigraphic height which corresponds to the
 569 colour legend to the right of the figure. Model solutions correspond to parameters presented in table S3, which was a
 570 scenario to explore changing diagenetic fluid (seawater) element concentrations to seek out a model fit to the lower
 571 Copper cap samples.

572
 573 Table S3: Model parameters to explain geochemistry of lower samples through changes in the chemical composition
 574 of seawater.

| Parameter | Definition | Value used in model |
|-----------|--|---|
| M_f | Chemical composition of diagenetic fluid (mmol/kg) | Ca = 3.0, Mg = 32.4, Li = 0.002 |
| M_s | Chemical composition of primary solid (aragonite) | Ca = 38%, C = 12%, Mg = 0.5%, Li = 0.13 ppm |

| | | | |
|------------|---|----|--|
| δ_f | Isotopic composition of diagenetic fluid | of | $\delta^{44/40}\text{Ca} = 0.0\text{‰}$, $\delta^{26}\text{Mg} = 0.1\text{‰}$, $\delta^7\text{Li} = 13\text{‰}$ |
| δ_s | Isotopic composition of primary solid (aragonite) | of | $\delta^{44/40}\text{Ca} = -1.5\text{‰}$, $\delta^{26}\text{Mg} = -$ 0.8‰ , $\delta^7\text{Li} = 1\text{‰}$ |

575

576 Although permissible in our calculations, the required shift in seawater [Ca] would be
 577 from 3 mmol/kg in the lower section to 19 mmol/kg in the middle section (compare Tables S2
 578 and S3). Because sedimentary facies do not dramatically change from the lower section to the
 579 middle section, we estimate the time captured across this transition by calculating a uniform
 580 deposition rate between previous geochronological constraints on the Coppercap Fm. and age-
 581 equivalent units and apply this depositional rate to the transition between lower samples and
 582 middle samples (Macdonald et al., 2010; Strauss et al., 2014; Rooney et al., 2014; MacLennan et
 583 al., 2017). With these constraints in place, it can be estimated that < 2 Myr is captured across this
 584 transition. Such a shift in [Ca] over the required timescale would not occur without significant
 585 implications for other aspects of the Earth system, which we discuss below.

586

587 The main sources of Ca to seawater is continental weathering of carbonate and silicate
 588 rocks and off-axis seafloor weathering reactions. The main removal mechanism of Ca from
 589 seawater is carbonate burial. An increase in the [Ca] of seawater could occur in response to an
 590 increase in Ca sources via enhanced weatherability or enhanced weathering rates, or a decrease
 591 in carbonate burial. Simply enhancing seawater [Ca] through increasing Ca input from
 592 continental or seafloor weathering (i.e., increasing weatherability) would lead to net CO₂
 593 drawdown and a reduction in global temperature which would buffer against increasing marine
 594 [Ca] through the slowing of weathering rates, and we can rule out such a scenario.

594

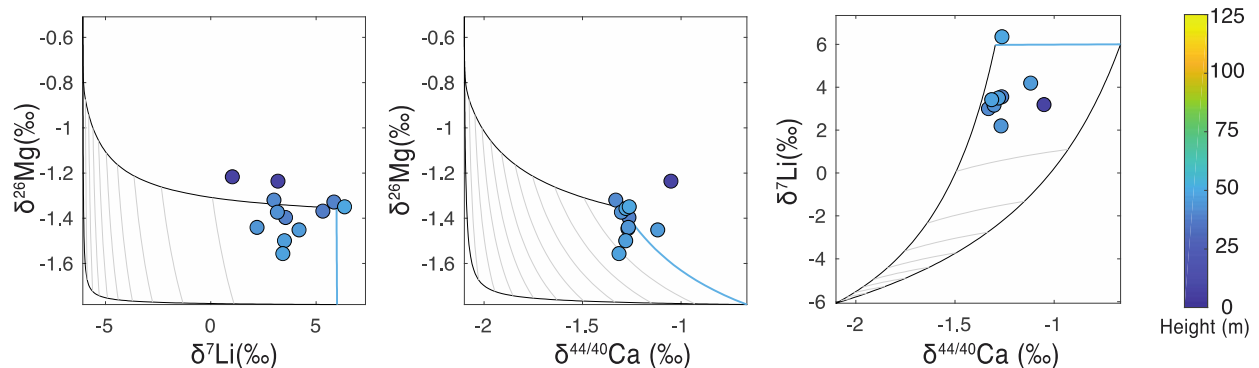
595 Alternatively, maintaining a constant Ca input to the oceans, we can estimate the
 596 reduction in carbonate burial needed to cause a 16 mmol increase in seawater [Ca]. Taking
 597 modern input and burial values and an initial [Ca] of 3 mmol/kg, an approximate 50% reduction
 598 in carbonate burial would be required to induce the required 16 mmol/kg shift in [Ca] over < 2
 599 Myrs. However, invoking a reduction in carbonate burial would ultimately lead to an increase in
 600 ocean alkalinity and drawdown of atmospheric CO₂, which would, in turn, reduce weathering
 601 rates and throttle the Ca supply. Therefore, this mechanism would require a CO₂ source
 602 concurrent with the reduction in carbonate burial. A massive injection of CO₂ into the ocean by
 603 large-scale organic matter respiration ($\delta^{13}\text{C} \sim -25\text{‰}$) or extreme volcanic outgassing ($\delta^{13}\text{C} \sim -6\text{‰}$)
 604 would cause a negative excursion in marine carbonate $\delta^{13}\text{C}$ values, inconsistent with the
 605 sedimentary record. Together these arguments weaken the case for a severe reduction in
 606 carbonate burial as a mechanism to increase seawater [Ca].

606

607 The above arguments leave enhanced volcanic CO₂ degassing as the only conceivable
 608 mechanism to dramatically increase [Ca] by ≈ 16 mmol/kg over our estimated time interval of < 2
 609 Myrs (higher temperature increases weathering rates). The isotopic consequences of such an
 610 injection are discussed above. Additionally, this mechanism is likely to result in dramatic
 611 changes to other components of the Earth surface, from increases to global surface temperature
 612 to changes in primary productivity and organic carbon burial. These changes would likely leave
 613 unambiguous signatures somewhere in the sedimentary record. To illustrate this point, if we
 614 again consider an extreme imbalance in which increases to Ca inputs do not increase Ca outputs,
 615 we would need to nearly double the Ca input flux to the ocean over the < 2 Myr interval between
 616 the lower and middle portions of the Coppercap Fm. Such a doubling of inputs, as discussed
 617 above, can only be achieved through enhancement of global weathering rates that requires an
 increase in surface temperature in response to increases in $p\text{CO}_2$. Using estimates of the

618 temperature dependence of weathering rates (e.g., Berner and Kothavala et al., 2001), such an
 619 increase in the Ca source would require approximately a doubling of atmospheric $p\text{CO}_2$. Such
 620 large, rapid shifts in atmospheric $p\text{CO}_2$ would likely require an extreme event, such as the
 621 eruption of a large igneous province (LIP). In the late Tonian a LIP eruption would be
 622 particularly necessary as it has been suggested that arc-volcanism was in a steady decline at this
 623 time (Mckenzie et al., 2016). However, geochronological constraints place the interval in
 624 question (between ≈ 735 -732 Ma), after notable events in the Tonian such as Katangan
 625 magmatism in the western Kalahari (~ 750 Ma), and before the eruption of the Franklin LIP
 626 (~ 723 Ma), making such a mechanism unlikely (Ernst et al., 2008). Finally, arguments above
 627 notwithstanding, it is important to note that such changes would require shifts in [Ca] to occur 1-
 628 2 orders of magnitude faster than documented across the Phanerozoic (Lowenstien et al., 2003;
 629 Horita et al., 2002). The above arguments make it difficult to justify invoking changes in silicate
 630 weathering to explain dramatic changes in seawater [Ca] between lower and middle portions of
 631 our section of the Coppercap Fm.

632
 633 **Changes in seawater isotopic composition are unlikely.** Model-measurement agreement in the
 634 lower section can also be achieved by varying the isotopic composition of seawater. Maintaining
 635 consistent element concentrations between lower, middle and upper portions of the Coppercap
 636 Fm. we can achieve model fits for the lower samples within $>80\%$ dolomitized fields by
 637 lowering the $\delta^{44/40}\text{Ca}$ and $\delta^7\text{Li}$ values of seawater by 0.6 and 7‰ respectively (Table S4; Fig.
 638 S3).
 639



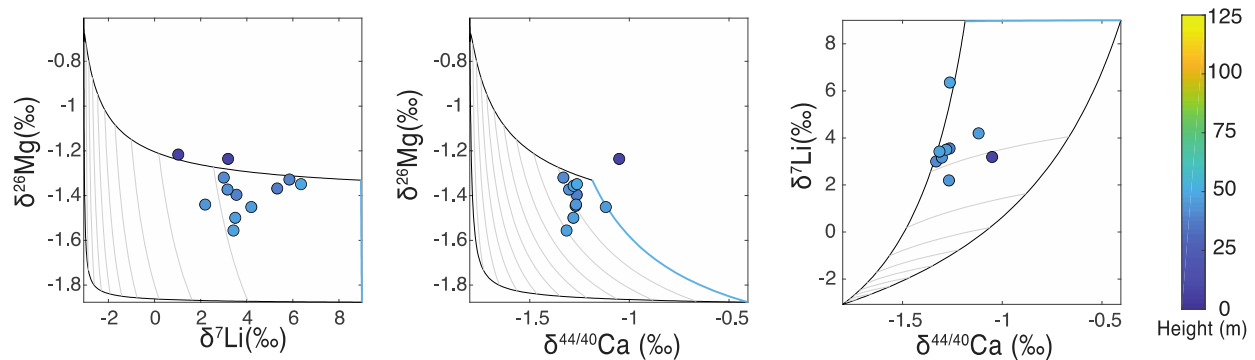
640
 641 Figure S3: $\delta^{26}\text{Mg}$ - $\delta^7\text{Li}$, $\delta^{26}\text{Mg}$ - $\delta^{44/40}\text{Ca}$ and $\delta^7\text{Li}$ - $\delta^{44/40}\text{Ca}$ cross-plots of both model solutions and data from the
 642 lower portion of the Coppercap Fm. The colours of data points represent stratigraphic height. Model solutions
 643 correspond to parameters presented in Table S4, which was a scenario to explore changing diagenetic fluid (seawater)
 644 isotopic compositions to seek out a model fit to the lower Coppercap Fm. samples.
 645

646 Table S4: Model parameters to explain geochemistry of lower samples through changes in isotopic compositions of
 647 seawater.

| Parameter | Definition | Value used in model |
|------------|--|--|
| M_f | Chemical composition of diagenetic fluid (mmol/kg) | Ca = 19.1, Mg = 43.2, Li = 0.002 |
| M_s | Chemical composition of primary solid (aragonite) | Ca = 39.5%, C = 12%, Mg = 1.03%, Li = 0.03 ppm |
| δ_f | Isotopic composition of diagenetic fluid | $\delta^{44/40}\text{Ca} = -0.6\text{‰}$, $\delta^{26}\text{Mg} = 0.2\text{‰}$, $\delta^7\text{Li} = 6\text{‰}$ |
| δ_s | Isotopic composition of primary solid (aragonite) | $\delta^{44/40}\text{Ca} = -1.5\text{‰}$, $\delta^{26}\text{Mg} = -0.8\text{‰}$, $\delta^7\text{Li} = 1\text{‰}$ |

648
649
650
651
652
653
654
655
656
657
658
659
660
661
662
663
664
665
666
667
668
669
670
671

The needed shifts in seawater isotopic composition are potentially possible through increases to congruent silicate weathering, which would suppress Li isotope fractionation during continental weathering, as well as near-complete quantitative uptake of Li at the locations of Li-sinks, which would suppress isotopic fractionation associated with such processes. Additionally, a seawater $\delta^7\text{Li}$ value as low as 7‰ predicts that some marine carbonates at this time would bear $\delta^7\text{Li} < 0\text{‰}$. Such low $\delta^7\text{Li}$ values have yet to be observed. In the case of Ca isotopes, lowering seawater $\delta^{44/40}\text{Ca}$ values to -0.6‰ could be achieved through lowering the $\delta^{44/40}\text{Ca}$ value of Ca inputs. This may be possible through weathering aragonite-dominated terrains exposed by dramatic sea level drop or through a non-steady state scenario where Ca inputs are not balanced by outputs, thereby shifting seawater $\delta^{44/40}\text{Ca}$ values closer to the Ca input compositions. Such a shift would likely occur with some indication in sedimentary facies, which is not observed in our section. Furthermore, with likely $\delta^{44/40}\text{Ca}$ values of the possible sources and sinks of Ca invoked to drive this change in seawater $\delta^{44/40}\text{Ca}$ values, the required fluxes of Ca are themselves substantial. For example, suspending carbonate burial altogether and achieving the decrease in seawater $\delta^{44/40}\text{Ca}$ values by weathering an aragonite platform, would increase [Ca] by almost 70%. If carbonate burial were ongoing, the time required for turnover of the marine Ca pool to affect a change of -0.6‰ would be long, relative to the time available in the Coppercap Fm. section. Therefore, arguments made above in the exploration of changes in [Ca] as the driver of the observed changes in the isotopic composition of diagenetic dolomite also weaken an explanation based on enhanced aragonite weathering. Even in a combined scenario (Table S5, Fig. S4), where we allow seawater to evolve isotopically and compositionally, the arguments presented above still apply, rendering such explanations difficult to support.



672
673
674
675
676
677
678
679

Figure S4: $\delta^{26}\text{Mg} - \delta^7\text{Li}$, $\delta^{26}\text{Mg} - \delta^{44/40}\text{Ca}$ and $\delta^7\text{Li} - \delta^{44/40}\text{Ca}$ cross-plots of both model solutions and data from the lower portion of the Coppercap Fm. The colours of data points represent stratigraphic height. Model solutions correspond to parameters presented in Table S5, which was a scenario to explore changing diagenetic fluid (seawater) chemical and isotopic compositions to seek out a model fit to the lower Coppercap Fm. samples.

Table S5: Model parameters to explain geochemistry of lower samples through changes in the chemical and isotopic compositions of seawater.

| Parameter | Definition | Value used in model |
|------------|--|---|
| M_f | Chemical composition of diagenetic fluid (mmol/kg) | Ca = 11.1, Mg = 35.1, Li = 0.002 |
| M_s | Chemical composition of primary solid (aragonite) | Ca = 39.5%, C = 12%, Mg = 1.03%, Li = 0.03 ppm |
| δ_f | Isotopic composition of diagenetic fluid | $\delta^{44/40}\text{Ca} = -0.3\text{‰}$, $\delta^{26}\text{Mg} = 0.2\text{‰}$, $\delta^7\text{Li} = 6\text{‰}$ |

| | | |
|------------|---|---|
| δ_s | Isotopic composition of primary solid (aragonite) | of $\delta^{44/40}\text{Ca} = -1.5\text{‰}$, $\delta^{26}\text{Mg} = -0.8\text{‰}$, $\delta^7\text{Li} = 1\text{‰}$ |
|------------|---|---|

680
681 While we cannot definitively rule out the above scenarios, all make predictions for
682 extreme changes in seawater chemistry across a < 2 Myr interval that should be expressed
683 globally. Moreover, such scenarios come along with additional implications beyond the cycles of
684 Ca, Mg and Li. As it is difficult to point to any obvious causes of such dramatic shifts, we
685 explore an alternative local explanation below.

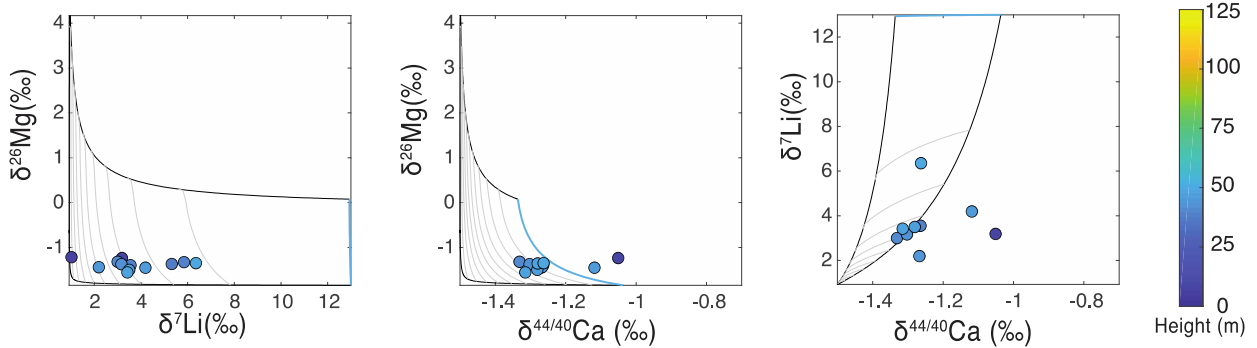
686
687 **A different diagenetic fluid may explain the isotopic composition of the lower section.** To
688 explore a scenario where seawater chemistry did not significantly change across the deposition
689 of the Coppercap Fm., we maintain the same initial aragonite geochemistry but alter the
690 composition of the diagenetic fluid that dolomitized the samples in the lower portion of the
691 section (Tables S6, S7 and S8). The best model fit to the data is achieved with a fluid with
692 lower Ca, Mg and Li concentrations and lower $\delta^{44/40}\text{Ca}$, $\delta^{26}\text{Mg}$ and $\delta^7\text{Li}$ values than the
693 proposed Tonian seawater (Table S8).

694 To deduce the origins of such a fluid we first consider the possibility that lower section
695 samples were diagenetically altered by a fluid that formed through the dilution of seawater with
696 meteoric fluids. However, since Li would only be sourced from seawater in this case, the
697 concentration and isotopic composition of Li in the meteoric-seawater mix do not allow
698 reproduction of the full range of observed $\delta^7\text{Li}$ values in model end-products that are >80%
699 dolomite, as required in the case of the Coppercap Fm. samples, which are fully dolomitized.

700 In the second case we consider a scenario where lower samples were dolomitized by a
701 fluid that formed through a mixture of seawater and terrestrial groundwaters at aragonite
702 saturation (Table S6). We first envision terrestrial groundwater flowing through an aragonite
703 aquifer, reaching saturation with the aragonite and then mixing with seawater at a freshwater-
704 seawater interface. We assign a Ca concentration and isotopic composition consistent with
705 aragonite dissolution until saturation is reached, and concentrations and isotopic compositions
706 of Mg and Li that reflect release from dissolving aragonite. The best-fit solution in this case is
707 also incapable of reproducing the range of observed $\delta^7\text{Li}$ values in model end-products that are
708 >80% dolomite (Fig. S5). Even in the case where we modify the chemistry of waters that
709 flowed into the aquifer allowing for different Ca:Mg:Li ratios (inferred from modern riverine
710 measurements flowing through silicate-dominated terrains; e.g., [Tipper et al., 2012](#)), we are still
711 unable to achieve a satisfactory model fit (Fig. S6, Table S7). Specifically, even when
712 modifying [Mg] and [Li] to ≈ 0.5 mM and 0.001 mM respectively (Table S7), many data points
713 are unable to be captured in >80% dolomite fields of a model solution.

714 The final option that we consider is that lower section samples were dolomitized in a
715 fluid that formed as mixture of seawater and a less saline fluid with approximately 2-3 times
716 less Mg, Li and Ca than contemporaneous seawater and lower $\delta^7\text{Li}$, $\delta^{26}\text{Mg}$ and $\delta^{44/40}\text{Ca}$
717 compositions (Table S8). Such a scenario is potentially analogous to modern settings such as
718 carbonate aquifers in Rottnest Island in Western Australia ([Martin et al., 2020](#)). Solutions
719 generated from this scenario fall close to the sediment-buffered end-member trajectory and
720 encapsulate most of the lower section data within model end-products that are >80% dolomite.
721 Given the diversity of possible sources of a solution of intermediate salinity, and the possibility
722 mixing between more than two end-member fluids, it is difficult to uniquely interpret this
723 scenario. However, allodapic carbonate facies strongly imply a marine slope environment for
724 original deposition of the lower section samples. In such an environment, the most likely

725 solution with which seawater may mix is brackish transition-zone water derived in part from
 726 interaction of continental waters with the sedimentary aquifer. Isotopically, such continentally-
 727 derived fluids may resemble fluids originating from weathering of silicate-dominated terrains,
 728 consistent with our hypothesized fluid composition (von Strandman et al., 2008; 2010;
 729 Hindshaw et al., 2013). Given its plausibility alongside its ability to fit the observations, we
 730 favor this scenario to explain the geochemistry of the lower portion of the Coppercap Fm.

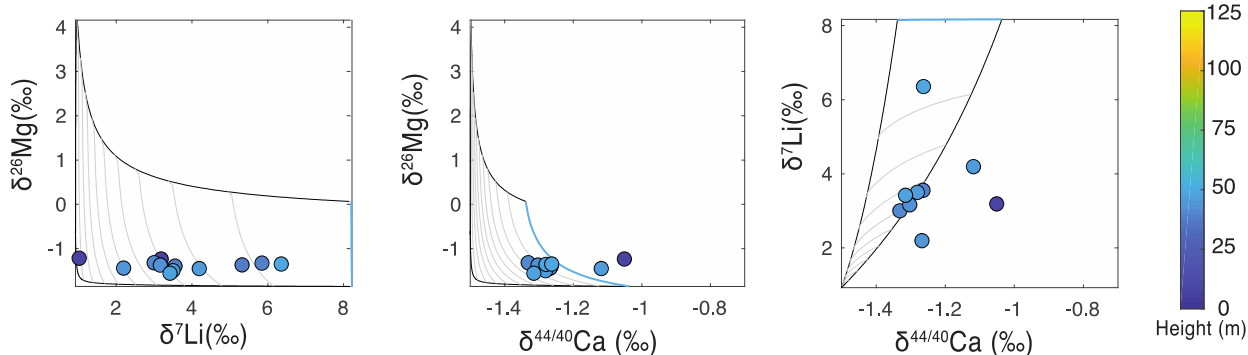


731 Figure S5: $\delta^{26}\text{Mg} - \delta^7\text{Li}$, $\delta^{26}\text{Mg} - \delta^{44/40}\text{Ca}$ and $\delta^7\text{Li} - \delta^{44/40}\text{Ca}$ cross-plots of both model solutions and data from the
 732 lower portion of the Coppercap Fm. The colours of data points represent stratigraphic height. Model solutions
 733 correspond to parameters presented in Table S6.
 734

735 Table S6: Model parameters to explain the geochemistry of lower samples through a groundwater influence on the
 736 chemical and isotopic composition of the dolomitizing fluid.
 737

| Parameter | Definition | Value used in model |
|-----------------------------------|--|---|
| M_{fd} | Chemical composition of diagenetic fluid (mmol/kg) | Ca = 7.0, Mg = 15.1, Li = 0.0007 |
| δ_{fd} | Isotopic composition of diagenetic fluid | $\delta^{44/40}\text{Ca} = -0.98\text{‰}$, $\delta^{26}\text{Mg} = 0.1\text{‰}$, $\delta^7\text{Li} = 13.0\text{‰}$ |
| M_{fsw} | Chemical composition of seawater (mmol/kg) | Ca = 19.1, Mg = 43.2, Li = 0.002 |
| M_s | Chemical composition of primary solid (aragonite) | Ca = 39.5%, C = 12%, Mg = 1.03%, Li = 0.03 ppm |
| δ_{fsw} | Isotopic composition of seawater | $\delta^{44/40}\text{Ca} = 0.0\text{‰}$, $\delta^{26}\text{Mg} = 0.1\text{‰}$, $\delta^7\text{Li} = 13\text{‰}$ |
| δ_s | Isotopic composition of primary solid (aragonite) | $\delta^{44/40}\text{Ca} = -1.5\text{‰}$, $\delta^{26}\text{Mg} = -0.6\text{‰}$, $\delta^7\text{Li} = 1\text{‰}$ |
| M_{fgw} | Chemical composition of groundwater (mmol/kg) | Ca = 0.5, Mg = 0.02, Li = 2×10^{-8} |
| δ_{fgw} | Isotopic composition of groundwater | $\delta^{44/40}\text{Ca} = -1.5\text{‰}$, $\delta^{26}\text{Mg} = -1.1\text{‰}$, $\delta^7\text{Li} = 1.0\text{‰}$ |
| Ratio of seawater to groundwaters | | 0.35 |

738
 739
 740
 741
 742

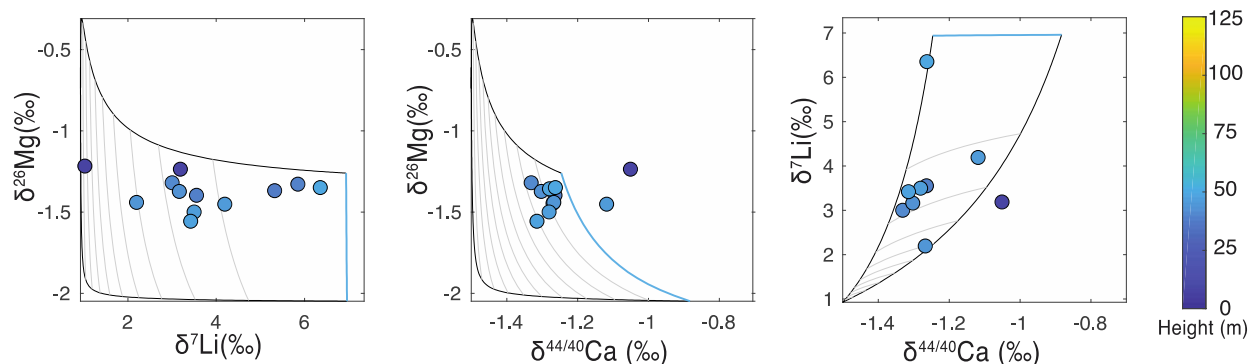


743
744 Figure S6 $\delta^{26}\text{Mg}$ - $\delta^7\text{Li}$, $\delta^{26}\text{Mg}$ - $\delta^{44/40}\text{Ca}$ and $\delta^7\text{Li}$ - $\delta^{44/40}\text{Ca}$ cross-plots of both model solutions and data from the
745 lower portion of the Coppercap Fm. The colours of data points represent stratigraphic height. Model solutions
746 correspond to parameters presented in Table S7.

747
748 Table S7: Model parameters to explain the geochemistry of lower samples through a groundwater influence on the
749 chemical and isotopic composition of the dolomitizing fluid.

| Parameter | Definition | Value used in model |
|-----------------------------------|--|--|
| M_{fd} | Chemical composition of diagenetic fluid (mmol/kg) | Ca = 7.0, Mg = 15.4, Li = 0.00135 |
| δ_{fd} | Isotopic composition of diagenetic fluid | $\delta^{44/40}\text{Ca} = -0.98\text{‰}$, $\delta^{26}\text{Mg} = 0.09\text{‰}$, $\delta^7\text{Li} = 6.48\text{‰}$ |
| M_{fsw} | Chemical composition of seawater (mmol/kg) | Ca = 19.1, Mg = 43.2, Li = 0.002 |
| M_s | Chemical composition of primary solid (aragonite) | Ca = 39.5%, C = 12%, Mg = 1.03%, Li = 0.03 ppm |
| δ_{fsw} | Isotopic composition of seawater | $\delta^{44/40}\text{Ca} = 0.0\text{‰}$, $\delta^{26}\text{Mg} = 0.1\text{‰}$, $\delta^7\text{Li} = 13\text{‰}$ |
| δ_s | Isotopic composition of primary solid (aragonite) | $\delta^{44/40}\text{Ca} = -1.5\text{‰}$, $\delta^{26}\text{Mg} = -0.6\text{‰}$, $\delta^7\text{Li} = 1\text{‰}$ |
| M_{fgw} | Chemical composition of groundwater (mmol/kg) | Ca = 0.5, Mg = 0.5, Li = 0.001 |
| δ_{fgw} | Isotopic composition of groundwater | $\delta^{44/40}\text{Ca} = -1.5\text{‰}$, $\delta^{26}\text{Mg} = -0.2\text{‰}$, $\delta^7\text{Li} = 3.0\text{‰}$ |
| Ratio of seawater to groundwaters | | 0.35 |

750
751
752
753



754

755 Figure S7: $\delta^{26}\text{Mg} - \delta^7\text{Li}$, $\delta^{26}\text{Mg} - \delta^{44/40}\text{Ca}$ and $\delta^7\text{Li} - \delta^{44/40}\text{Ca}$ cross-plots of both model solutions and data from the
 756 lower portion of the Coppercap Fm. The colours of data points represent stratigraphic height. Model solutions
 757 correspond to parameters presented in Table S8.
 758

759 Table S8: Model parameters to explain the geochemistry of lower samples through a brackish transitional water
 760 influence on the chemical and isotopic composition of the dolomitizing fluid.

| Parameter | Definition | Value used in model |
|---|--|---|
| M_{fd} | Chemical composition of diagenetic fluid (mmol/kg) | Ca = 10.0, Mg = 26.5, Li = 0.00125 |
| δ_{fd} | Isotopic composition of diagenetic fluid | $\delta^{44/40}\text{Ca} = -0.83\text{‰}$, $\delta^{26}\text{Mg} = -0.08\text{‰}$, $\delta^7\text{Li} = 6.96\text{‰}$ |
| M_{fsw} | Chemical composition of seawater (mmol/kg) | Ca = 19.1, Mg = 43.2, Li = 0.002 |
| M_s | Chemical composition of primary solid (aragonite) | Ca = 39.5%, C = 12%, Mg = 1.03%, Li = 0.03 ppm |
| δ_{fsw} | Isotopic composition of seawater | $\delta^{44/40}\text{Ca} = 0.0\text{‰}$, $\delta^{26}\text{Mg} = 0.1\text{‰}$, $\delta^7\text{Li} = 13\text{‰}$ |
| δ_s | Isotopic composition of primary solid (aragonite) | $\delta^{44/40}\text{Ca} = -1.5\text{‰}$, $\delta^{26}\text{Mg} = -0.6\text{‰}$, $\delta^7\text{Li} = 1\text{‰}$ |
| M_{fgw} | Chemical composition of brackish transitional waters (mmol/kg) | Ca = 7.0, Mg = 21.0, Li = 0.001 |
| δ_{fgw} | Isotopic composition of Brackish Transitional Waters | $\delta^{44/40}\text{Ca} = -1.1\text{‰}$, $\delta^{26}\text{Mg} = -0.2\text{‰}$, $\delta^7\text{Li} = 3.0\text{‰}$ |
| Ratio of seawater to brackish transitional waters | | 0.25 |

761
 762
 763 Data table S9: Geochemical results.
 764

| Sample | d13C | d18O | d44/40 Ca vs SW | d26/24 Mg vs DSM 3 | d7Li vs LSVEC | Mg (mol/mol Ca) | Sr (mmol/mol Ca) | Mn (mmol/mol Ca) | Li ($\mu\text{mol/mol Ca}$) |
|-----------|-------|-------|-----------------|--------------------|---------------|-----------------|------------------|------------------|-------------------------------|
| M303-6.0 | -4.49 | -3.50 | | -1.22 | 1.03 | 0.84 | 0.34 | 5.48 | 1.81 |
| M303-6.8 | -4.95 | -3.77 | -1.05 | -1.24 | 3.19 | 0.84 | 0.42 | 5.37 | 8.78 |
| M303-36.6 | -3.24 | -2.71 | | -1.37 | 5.32 | 0.97 | 0.20 | 0.50 | 1.42 |
| M303-37.4 | -3.22 | -3.19 | -1.26 | -1.40 | 3.55 | 0.97 | 0.25 | 0.54 | 1.21 |
| M303-38.3 | -3.09 | -3.08 | | -1.33 | 5.85 | 0.97 | 0.23 | 0.72 | 0.72 |
| M303-40.5 | -2.13 | -2.82 | -1.33 | -1.32 | 3.00 | 1.00 | 0.17 | 0.90 | 7.47 |
| M303-41.4 | -2.07 | -2.87 | -1.27 | -1.45 | | 0.98 | 0.16 | 0.87 | 1.35 |
| M303-42.5 | -2.03 | -2.54 | -1.30 | -1.37 | 3.16 | 0.96 | 0.18 | 1.56 | 1.15 |
| M303-43.6 | -1.64 | -3.26 | -1.27 | -1.44 | 2.20 | 0.99 | 0.17 | 1.40 | 1.87 |
| M303-44.8 | -1.43 | -1.82 | -1.12 | -1.45 | 4.19 | 1.02 | 0.16 | 1.58 | 1.82 |
| M303-45.9 | -0.39 | -3.31 | -1.28 | -1.50 | 3.50 | 0.93 | 0.14 | 1.37 | 1.23 |
| M303-46.7 | -1.89 | -0.91 | -1.32 | -1.56 | 3.42 | 0.99 | 0.16 | 0.77 | 2.14 |
| M303-48 | -0.44 | -1.83 | -1.28 | -1.36 | | 0.98 | 0.24 | 1.04 | 0.15 |
| M303-49 | 0.30 | -1.88 | -1.26 | -1.35 | 6.35 | 0.99 | 0.14 | 0.89 | 0.97 |
| M303-50.3 | 0.37 | -2.07 | -1.20 | -1.40 | | 0.97 | 0.17 | 1.37 | 0.90 |
| M303-51.1 | -0.13 | 2.26 | -1.18 | -1.57 | 7.79 | 0.99 | 0.15 | 0.92 | 2.00 |
| M303-52 | 0.63 | 0.78 | -1.14 | -1.50 | 7.88 | 0.97 | 0.15 | 1.33 | 1.65 |
| M303-53.7 | 0.51 | -2.08 | -1.14 | -1.39 | 8.46 | 1.01 | 0.15 | 1.84 | 2.42 |
| M303-54.5 | 0.72 | 0.54 | -1.12 | -1.61 | 7.22 | 1.00 | 0.15 | 2.24 | 2.04 |
| M303-55.9 | 0.13 | 0.48 | -1.01 | -1.95 | 8.92 | 1.00 | 0.13 | 1.27 | 2.05 |
| M303-57 | 0.42 | 1.62 | -0.98 | -1.78 | 9.59 | 0.98 | 0.13 | 1.65 | 1.46 |
| M303-57.9 | 0.43 | 1.40 | -0.78 | -1.66 | 9.51 | 1.00 | 0.12 | 1.34 | 1.15 |

| | | | | | | | | | |
|------------|-------|--------|-------|-------|-------|------|------|------|-------|
| M303-59.2 | 1.21 | 2.17 | -0.86 | -1.72 | 9.22 | 1.01 | 0.14 | 1.99 | 1.83 |
| M303-59.9 | 0.60 | -0.02 | | -1.61 | 9.19 | 1.02 | 0.14 | 1.33 | 1.88 |
| M303-62.5 | 0.83 | -1.74 | -0.65 | -1.67 | 9.73 | 1.00 | 0.12 | 1.31 | 1.28 |
| M303-63.3 | 0.87 | -4.16 | -0.89 | -1.50 | 8.27 | 1.00 | 0.15 | 1.87 | 1.77 |
| M303-67.3 | 0.87 | -0.49 | -0.78 | -1.59 | 9.62 | 1.01 | 0.12 | 1.81 | 1.90 |
| M303-68 | 0.96 | -3.26 | -0.77 | -1.41 | 7.91 | 1.00 | 0.13 | 1.92 | 1.70 |
| M303-69 | 0.72 | -2.57 | -0.85 | -1.68 | | 1.04 | 0.18 | 2.32 | 1.76 |
| M303-70.7 | 0.63 | -5.62 | -0.60 | -1.80 | 8.68 | 1.03 | 0.17 | 1.01 | 1.67 |
| M303-71.1 | 0.54 | -4.22 | | -1.68 | 8.40 | 1.04 | 0.18 | 0.99 | 1.82 |
| M303-72.6 | 0.44 | -5.74 | -0.25 | -1.80 | 9.52 | 1.02 | 0.24 | 0.45 | 1.69 |
| M303-73.6 | 0.96 | -1.21 | -0.37 | -1.88 | 11.31 | 0.99 | 0.32 | 0.48 | 1.40 |
| M303-74.6 | 1.05 | -1.38 | -0.55 | | | 1.01 | 0.28 | 0.67 | 1.56 |
| M303-75.6 | 1.06 | -2.52 | | -1.74 | | 1.01 | 0.25 | 0.50 | 0.53 |
| M303-76.6 | 0.86 | -2.94 | -0.48 | -1.70 | 11.96 | 1.05 | 0.24 | 0.56 | 1.35 |
| M303-77.7 | 0.55 | -6.03 | -0.82 | -1.69 | 9.85 | 1.01 | 0.22 | 0.61 | 1.31 |
| M303-79.3 | 0.86 | -1.57 | -0.71 | -1.76 | 8.32 | 1.01 | 0.28 | 0.57 | 1.09 |
| M303.80.2 | 0.69 | -4.35 | -0.61 | -1.61 | 12.04 | 1.03 | 0.29 | 0.56 | 0.74 |
| M303-81.6 | 1.14 | -2.10 | -0.56 | -1.69 | 12.73 | 1.01 | 0.32 | 0.35 | 1.96 |
| M303-83.1 | 1.27 | -1.43 | -0.41 | -1.85 | 8.49 | 1.03 | 0.29 | 0.15 | 1.65 |
| M303-84.4 | 1.14 | -3.19 | -0.70 | -1.91 | 5.94 | 1.06 | 0.18 | 0.12 | 0.50 |
| M303-86.6 | -0.34 | -3.23 | | | 10.68 | 1.00 | 0.23 | 0.20 | 2.29 |
| M303-88.6 | -0.26 | -8.45 | -0.93 | -1.13 | 8.04 | 0.97 | 0.13 | 0.38 | 1.64 |
| M303-90.1 | -0.27 | -9.85 | -0.94 | -1.14 | 6.35 | 0.99 | 0.14 | 0.95 | 1.55 |
| M303-92.6 | -0.07 | -1.59 | -0.85 | -1.06 | 8.48 | 0.92 | 0.21 | 0.49 | 0.69 |
| M303-93.6 | 0.90 | -8.64 | -0.72 | -1.53 | 3.96 | 0.99 | 0.23 | 0.51 | 1.12 |
| M303-94.6 | 1.36 | -7.55 | -0.55 | -1.50 | | 1.02 | 0.17 | 0.39 | 0.83 |
| M303-96.2 | 0.67 | -11.29 | -0.83 | -1.27 | 8.12 | 1.00 | 0.12 | 0.83 | 0.97 |
| M303-97.9 | 0.37 | -11.63 | -0.94 | -1.23 | 7.71 | 0.98 | 0.10 | 0.52 | 1.48 |
| M303-99.5 | 1.09 | -12.17 | -1.13 | -0.91 | | 0.95 | 0.10 | 3.25 | 10.01 |
| M303-100.6 | 1.21 | -12.48 | -0.90 | -0.95 | 6.07 | 0.99 | 0.08 | 1.67 | 0.62 |
| M303-101.9 | 0.70 | -11.62 | -0.92 | -1.27 | 8.55 | 0.99 | 0.13 | 0.72 | 0.86 |
| M303-102.8 | 0.40 | -11.68 | -0.85 | -1.16 | | 0.97 | 0.09 | 0.78 | 0.38 |
| M303-104.3 | 2.49 | -12.86 | -1.03 | -0.85 | 6.17 | 0.98 | 0.07 | 1.30 | 0.69 |
| M303-105.6 | 3.06 | -13.39 | -0.77 | -0.57 | 4.98 | 0.97 | 0.11 | 1.45 | 0.50 |
| M303-106.3 | 2.70 | -13.17 | -1.09 | -0.68 | | 0.96 | 0.08 | 1.79 | 0.57 |
| M303-107.7 | 2.75 | -12.92 | -1.07 | -0.94 | 7.56 | 1.00 | 0.07 | 1.78 | 0.70 |
| M303-109.4 | 1.26 | -11.99 | -0.93 | -0.99 | 7.25 | 1.01 | 0.10 | 0.83 | 0.44 |
| M303-110.6 | 1.02 | -12.59 | -0.90 | -1.04 | 7.52 | 0.96 | 0.06 | 0.44 | 1.41 |
| M303-111.5 | 2.24 | -13.13 | -1.13 | -0.87 | 6.30 | 1.00 | 0.09 | 3.28 | 0.65 |
| M303-113.4 | 3.49 | -12.86 | -0.97 | -0.62 | 6.79 | 0.97 | 0.09 | 1.95 | 0.56 |
| M303-115.6 | 3.84 | -13.12 | -1.12 | -0.71 | 5.00 | 0.97 | 0.06 | 1.84 | 1.81 |
| M303-117.6 | 3.35 | -12.22 | -0.83 | -1.28 | 8.20 | 1.01 | 0.12 | 0.47 | 8.78 |
| M303-118.8 | 3.51 | -11.85 | -0.83 | -1.60 | 8.25 | 0.99 | 0.09 | 0.50 | 1.42 |
| M303-123.1 | 0.58 | -5.10 | -0.96 | -1.20 | 9.60 | 0.95 | 0.13 | 0.34 | 1.21 |
| M303-125.1 | | | -0.99 | -1.20 | 7.35 | 0.98 | 0.10 | 0.60 | 0.72 |
| M303-125.7 | | | -0.70 | -1.30 | 7.19 | 0.98 | 0.11 | 0.66 | 7.47 |

765
766
767
768
769
770
771
772
773
774

775
776
777
778
779
780
781
782
783
784
785
786
787
788
789
790
791
792
793
794
795
796
797
798
799
800
801
802
803
804
805
806
807
808
809
810
811
812
813
814
815
816
817
818
819
820
821
822
823

References:

1. Caro, G., Papanastassiou, D.A. and Wasserburg, G.J., 2010, 40K–40Ca isotopic constraints on the oceanic calcium cycle: *Earth and Planetary Science Letters*, 296(1-2), pp.124-132.
2. Young, E.D., Galy, A. and Nagahara, H., 2002, Kinetic and equilibrium mass-dependent isotope fractionation laws in nature and their geochemical and cosmochemical significance: *Geochimica et Cosmochimica Acta*, 66(6), pp.1095-1104.
3. Heuser, A. and Eisenhauer, A., 2008, The calcium isotope composition ($\delta^{44}/^{40}\text{Ca}$) of NIST SRM 915b and NIST SRM 1486: *Geostandards and Geoanalytical Research*, 32(3), pp.311-315.
4. Ahm, A.S.C., Bjerrum, C.J., Blättler, C.L., Swart, P.K. and Higgins, J.A., 2018, Quantifying early marine diagenesis in shallow-water carbonate sediments: *Geochimica et Cosmochimica Acta*, 236, pp.140-159.
5. Higgins, J.A. et al., 2018, Mineralogy, early marine diagenesis, and the chemistry of shallow-water carbonate sediments: *Geochimica et Cosmochimica Acta*, 220, pp.512-534.
6. Dellinger, M., Hardisty, D.S., Planavsky, N.J., Gill, B.C., Calderon-Asael, B., Asael, D., Croissant, T., Swart, P.K. and West, A.J., 2020, The effects of diagenesis on lithium isotope ratios of shallow marine carbonates: *American Journal of Science*, 320(2), pp.150-184.
7. Taylor, H., Kell-Duivesteyn, I., Farkas, J., Dietzel, M. and Dosseto, A., 2019, Lithium isotopes in dolostone as a palaeo-environmental proxy-an experimental approach: *Climates of the Past* (15) pp. 635-646
8. Langer, G., Sadekov, A., Thoms, S., Mewes, A., Nehrke, G., Greaves, M., Misra, S., Bijma, J. and Elderfield, H., 2015, Li partitioning in the benthic foraminifera *Ampistegina lessonii*: *Geochemistry, Geophysics, Geosystems*, 16(12), pp.4275-4279.
9. Langer, G., Sadekov, A., Greaves, M., Nehrke, G., Probert, I., Misra, S. and Thoms, S., 2020, Li partitioning into coccoliths of *Emiliania huxleyi*: evaluating the general role of “vital effects” in explaining element partitioning in biogenic carbonates: *Geochemistry, Geophysics, Geosystems*, 21(8), p.e2020GC009129.
10. Jacobson, A.D. and Holmden, C., 2008, $\delta^{44}\text{Ca}$ evolution in a carbonate aquifer and its bearing on the equilibrium isotope fractionation factor for calcite: *Earth and Planetary Science Letters*, 270(3-4), pp.349-353.

- 824
825
826
827
828
829
830
831
832
833
834
835
836
837
838
839
840
841
842
843
844
845
846
847
848
849
850
851
852
853
854
855
856
857
858
859
860
861
862
863
864
865
866
867
868
869
870
871
872
873
874
875
876
877
11. Fantle, M.S. and DePaolo, D.J., 2007, Ca isotopes in carbonate sediment and pore fluid from ODP Site 807A: the Ca²⁺ (aq)–calcite equilibrium fractionation factor and calcite recrystallization rates in Pleistocene sediments: *Geochimica et Cosmochimica Acta*, 71(10), pp.2524-2546.
 12. Fantle, M.S. and Higgins, J., 2014, The effects of diagenesis and dolomitization on Ca and Mg isotopes in marine platform carbonates: implications for the geochemical cycles of Ca and Mg: *Geochimica et Cosmochimica Acta*, 142, pp.458-481.
 13. Horita, J., 2014, Oxygen and carbon isotope fractionation in the system dolomite–water–CO₂ to elevated temperatures: *Geochimica et Cosmochimica Acta*, 129, pp.111-124.
 14. Gussone, N., Ahm, A.S.C., Lau, K.V. and Bradbury, H.J., 2020, Calcium isotopes in deep time: Potential and limitations: *Chemical Geology*, p.119601.
 15. Wang, Z., Hu, P., Gaetani, G., Liu, C., Saenger, C., Cohen, A. and Hart, S., 2013, Experimental calibration of Mg isotope fractionation between aragonite and seawater. *Geochimica et Cosmochimica Acta*, 102, pp.113-123.
 16. Romanek, C.S., Grossman, E.L. and Morse, J.W., 1992, Carbon isotopic fractionation in synthetic aragonite and calcite: effects of temperature and precipitation rate: *Geochimica et cosmochimica acta*, 56(1), pp.419-430.
 17. Dellinger, M., West, A.J., Paris, G., Adkins, J.F., von Strandmann, P.A.P., Ullmann, C.V., Eagle, R.A., Freitas, P., Bagard, M.L., Ries, J.B. and Corsetti, F.A., 2018, The Li isotope composition of marine biogenic carbonates: Patterns and Mechanisms: *Geochimica et Cosmochimica Acta*, 236, pp.315-335.
 18. von Strandmann, P.A.P., Schmidt, D.N., Planavsky, N.J., Wei, G., Todd, C.L. and Baumann, K.H., 2019, Assessing bulk carbonates as archives for seawater Li isotope ratios: *Chemical Geology*, 530, p.119338.
 19. Marriott, C.S., Henderson, G.M., Crompton, R., Staubwasser, M. and Shaw, S., 2004, Effect of mineralogy, salinity, and temperature on Li/Ca and Li isotope composition of calcium carbonate: *Chemical Geology*, 212(1-2), pp.5-15.
 20. Fantle, M.S. and Tipper, E.T., 2014, Calcium isotopes in the global biogeochemical Ca cycle: Implications for development of a Ca isotope proxy: *Earth-Science Reviews*, 129, pp.148-177.
 21. Swart, P.K., Ruiz, J. and Holmes, C.W., 1987. Use of strontium isotopes to constrain the timing and mode of dolomitization of upper Cenozoic sediments in a core from San Salvador, Bahamas: *Geology*, 15(3), pp.262-265.
 22. Henderson, G.M., Slowey, N.C. and Haddad, G.A., 1999, Fluid flow through carbonate platforms: constraints from ²³⁴U/²³⁸U and Cl⁻ in Bahamas pore-waters: *Earth and Planetary Science Letters*, 169(1-2), pp.99-111.
 23. Macdonald, F.A., Schmitz, M.D., Crowley, J.L., Roots, C.F., Jones, D.S., Maloof, A.C., Strauss, J.V., Cohen, P.A., Johnston, D.T. and Schrag, D.P., 2010, Calibrating the Cryogenian: *Science*, 327(5970), pp.1241-1243.
 24. Strauss, J.V., Rooney, A.D., Macdonald, F.A., Brandon, A.D. and Knoll, A.H., 2014, 740 Ma vase-shaped microfossils from Yukon, Canada: Implications for Neoproterozoic chronology and biostratigraphy: *Geology*, 42(8), pp.659-662.
 25. Rooney, A.D., Macdonald, F.A., Strauss, J.V., Dudás, F.Ö., Hallmann, C. and Selby, D., 2014, Re-Os geochronology and coupled Os-Sr isotope constraints on the Sturtian snowball Earth: *Proceedings of the National Academy of Sciences*, 111(1), pp.51-56.
 26. MacLennan, S., Park, Y., Swanson-Hysell, N., Maloof, A., Schoene, B., Gebreslassie, M., Antilla, E., Tesema, T., Alene, M. and Haileab, B., 2018, The arc of the Snowball: U-Pb dates constrain the Islay anomaly and the initiation of the Sturtian glaciation: *Geology*, 46(6), pp.539-542.
 27. Berner, R.A. and Kothavala, Z., 2001, GEOCARB III: a revised model of atmospheric CO₂ over Phanerozoic time: *American Journal of Science*, 301(2), pp.182-204.
 28. McKenzie, N.R., Horton, B.K., Loomis, S.E., Stockli, D.F., Planavsky, N.J. and Lee, C.T.A., 2016, Continental arc volcanism as the principal driver of icehouse-greenhouse variability: *Science*, 352(6284), pp.444-447.
 29. Ernst, R.E., Wingate, M.T.D., Buchan, K.L. and Li, Z.X., 2008. Global record of 1600–700 Ma Large Igneous Provinces (LIPs): implications for the reconstruction of the proposed Nuna (Columbia) and Rodinia supercontinents: *Precambrian Research*, 160(1-2), pp.159-178.
 30. Lowenstein, T.K., Hardie, L.A., Timofeeff, M.N. and Demicco, R.V., 2003, Secular variation in seawater chemistry and the origin of calcium chloride basinal brines: *Geology*, 31(10), pp.857-860.

- 878
879
880
881
882
883
884
885
886
887
888
889
890
891
892
893
894
895
896
31. Horita, J., Zimmermann, H. and Holland, H.D., 2002, Chemical evolution of seawater during the Phanerozoic: Implications from the record of marine evaporites: *Geochimica et Cosmochimica Acta*, 66(21), pp.3733-3756.
 32. Tipper, E.T., Lemarchand, E., Hindshaw, R.S., Reynolds, B.C. and Bourdon, B., 2012, Seasonal sensitivity of weathering processes: Hints from magnesium isotopes in a glacial stream: *Chemical Geology*, 312, pp.80-92.
 33. Martin, A.N., Meredith, K., Norman, M.D., Bryan, E. and Baker, A., 2020, Lithium and strontium isotope dynamics in a carbonate island aquifer, Rottnest Island, Western Australia: *Science of The Total Environment*, 715, p.136906.
 34. von Strandmann, P.A.P., Burton, K.W., James, R.H., van Calsteren, P., Gislason, S.R. and Sigfússon, B., 2008, The influence of weathering processes on riverine magnesium isotopes in a basaltic terrain: *Earth and Planetary Science Letters*, 276(1-2), pp.187-197.
 35. von Strandmann, P.A.P., Burton, K.W., James, R.H., van Calsteren, P. and Gislason, S.R., 2010, Assessing the role of climate on uranium and lithium isotope behaviour in rivers draining a basaltic terrain: *Chemical Geology*, 270(1-4), pp.227-239.
 36. Hindshaw, R.S., Reynolds, B.C., Wiederhold, J.G., Kretzschmar, R. and Bourdon, B., 2011, Calcium isotopes in a proglacial weathering environment: Damma glacier, Switzerland: *Geochimica et Cosmochimica Acta*, 75(1), pp.106-118.